(12) LEVEL III AD-E300519

AD A069155

DNA 4720F

DEVELOPMENT OF AN INTENSE ELECTRON BEAM ENVIRONMENT FOR MATERIAL CHARACTERIZATION

Physics International Company
2700 Merced Street
San Leandro, California 94577

October 1978

Final Report for Period 1 September 1976—27 October 1978

CONTRACT No. DNA 001-76-C-0362

APPROVED FOR PUBLIC RELEASE;
DISTRIBUTION UNLIMITED.

DDC
RECEIVED
MAY 30 1979
B

Prepared for
Director
DEFENSE NUCLEAR AGENCY
Washington, D. C. 20305

79 04 26 407

Destroy this report when it is no longer
needed. Do not return to sender.

62704H

REPORT DOCUMENTATION PAGE		READ INSTRUCTIONS BEFORE COMPLETING FORM
1. REPORT NUMBER DNA 4720F	2. GOVT ACCESSION NO.	3. RECIPIENT'S CATALOG NUMBER
4. TITLE *(and Subtitle)* DEVELOPMENT OF AN INTENSE ELECTRON BEAM ENVIRONMENT FOR MATERIAL CHARACTERIZATION		5. TYPE OF REPORT & PERIOD COVERED Final Report for Period 1 Sep 76—27 Oct 78
		6. PERFORMING ORG. REPORT NUMBER PIFR-21-979
7. AUTHOR(s) D. Dakin		8. CONTRACT OR GRANT NUMBER(s) DNA 001-76-C-0362
9. PERFORMING ORGANIZATION NAME AND ADDRESS Physics International Company 2700 Merced Street San Leandro, California 94577		10. PROGRAM ELEMENT, PROJECT, TASK AREA & WORK UNIT NUMBERS NWED Subtask N99QAXAA121-12
11. CONTROLLING OFFICE NAME AND ADDRESS Director Defense Nuclear Agency Washington, D.C. 20305		12. REPORT DATE October 1978
		13. NUMBER OF PAGES 66
14. MONITORING AGENCY NAME & ADDRESS*(if different from Controlling Office)*		15. SECURITY CLASS *(of this report)* UNCLASSIFIED
		15a. DECLASSIFICATION/DOWNGRADING SCHEDULE

16. DISTRIBUTION STATEMENT *(of this Report)*

Approved for public release; distribution unlimited.

17. DISTRIBUTION STATEMENT *(of the abstract entered in Block 20, if different from Report)*

19. KEY WORDS *(Continue on reverse side if necessary and identify by block number)*

Intense Beams	Rel. Electron Beam Angles
Magnetic Beam Compression	Rel. Elect. Beam Diagnostics
Relativistic Electron Beams	Electron Beam-Material Characterization
Materials Response	

20. ABSTRACT *(Continue on reverse side if necessary and identify by block number)*

An intense relativistic electron beam environment has been developed for material characterization. Experimental results on the magnetic compression and expansion of intense beams are presented and compared with theoretical models; emphasis is given to transport efficiency, electron angular distributions, and beam uniformity. Diode energies of 75 kJ are achieved (DNA OWL II generator) with greater than 80 percent transport efficiency using a magnetic compression ratio of three. Experimental results

over?

20. ABSTRACT (Continued)

results have been analyzed in terms of the physics of diode impedance
lifetime. Several diagnostics essential for characterizing these intense
beams have been successfully demonstrated.

ACCESSION for

NTIS	White Section
DDC	Buff Section ☐
UNANNOUNCED	☐
JUSTIFICATION	

BY

DISTRIBUTION/AVAILABILITY CODES

Dist.	AVAIL. and/or SPECIAL
A	

CONTENTS

ILLUSTRATIONS

ILLUSTRATIONS (cont.)

SECTION 1
INTRODUCTION

The objectives of this program were to develop diode and beam transport capabilities (using the DNA OWL II generator), which can achieve 1500 cal/gm over areas of $\geqslant 10$ cm^2 with mean electron voltages of 1 MV. These objectives were achieved and in fact were exceeded both in dose (up to 3000 to 4000 cal/gm) and in area (greater than 25 cm^2). In developing this capability, several diagnostics were to be investigated to determine their potential for characterizing diode and beam parameters in this intense environment. A range of diagnostics was successfully developed and tested and have been used in subsequent follow-on programs.

Several earlier experiments to generate intense beams were attempted with small-area diodes (cathode areas 40 to 100 cm^2) in applied magnetic fields; these experiments were characterized by erratic diode behavior and insulator breakdown. The major limitations on diode behavior were prepulse effects and impedance lifetime due to electrode plasma closure velocities. In this program these limitations were investigated. In the past, the relationship between closure velocity and beam parameters (V, J, τ, etc.) was not well understood. The results of this program were used to verify analyses of OWL II diodes that correlated impedance collapse with anode plasma formation and beam energy density. From this analysis an 80 cm^2 cathode was selected with magnetic beam compression utilized to achieve the required fluence and dose. Diode

5

energies were increased from 25 to 35 kJ (previous programs) to 50 to 75 kJ with mean voltages of up to 1 MV. The fluence at the diode (150 to 200 cal/cm^2) was then compressed by a factor of three with greater than 80 percent transport efficiency to the sample region. Prepulse effects were studied using surface flashover switches in the cathode with improvements obtained in both reliability and beam uniformity. Insulator breakdown problems were relieved by reducing inductance in the vacuum feed region of the load. However, some improvements still need to be addressed in late time insulator flashes, which reduce diode energy.

Magnetic beam compression is a key element of relativistic electron beams for material response applications. This program has yielded experimental support to theories generated at PI on magnetic compression of intense beams. Magnetic compression not only provides the required high dose levels but by subsequent beam expansion the results of this program have shown that lower mean angle beams than could be obtained without compression can be generated at larger areas for intermediate to low dose levels. Initial studies of electron angle for intense beams including both analysis and experimental measurements were an important part of the present program.

The diagnostics included in this program were a single channel Faraday cup and total fluence calorimeter for charge and energy transport efficiency and, more importantly, a filtered Faraday cup for obtaining electron beam angle at high doses through measurements of the charge deposition profile. Other diagnostics included were an X-ray pinhole camera and segmented calorimeter for beam fluence and uniformity and foil calorimeter for beam angle at low dose locations.

6

In summary this program has verified magnetic beam compression at very high dose levels, added to our capability and understanding of compression of intense beams, increased our understanding of the physics of diode impedance lifetime, and demonstrated several diagnostics essential for characterizing relativistic electron beams for material response applications.

Section 2 presents an analysis of the physics involved in magnetic compression of intense beams with an emphasis on the associated electron angular distributions. The experimental apparatus is described in Section 3. This is followed by experimental results on diode impedance and transport efficiencies in Section 4. Section 5 presents measurements of beam uniformity and initial determinations of electron angles.

SECTION 2

ANALYSIS OF BEAM GENERATION AND MAGNETIC COMPRESSION

2.1 MAGNETIC COMPRESSION OF INTENSE BEAMS

In the last two years there have been several advancements in the understanding of magnetic compression of intense beams. Earlier experiments on compression at PI and as reported in the literature (e.g. References 1-6), showed that the beam area predictably decreases in proportion to the ratio of magnetic field strength. Measured beam transmissions through converging magnetic fields, however, were in conflict with our understanding of beam properties in the diode. A theoretical analysis for magnetic compression of intense beams has been published by T. S. Young and P. Spence (Reference 7). Their theory agrees with the experimental results existing at the time of publication, but much of that data was taken at low beam energies and consequently did not completely test the theory. The results of the program reported here provide substantial support to that theory for intense beams.

To magnetically compress intense electron beams, an axial B_z field is applied with field strength increasing and then decreasing in the direction of beam propagation. The principles involved in the magnetic compression of intense electron beams are schematically illustrated in Figure 2.1. First we consider the region between the diode and position of the maximum magnetic field. In the diode one has both the applied magnetic field (B_z) and the

B_T

$B_T = B_Z$

DIODE

TRANSPORT

FARADAY CUP
FILTERED FARADAY CUP
CALORIMETRY
X-RAY PHOTOGRAPHY
DEPTH DOSE, CALORIMETRY
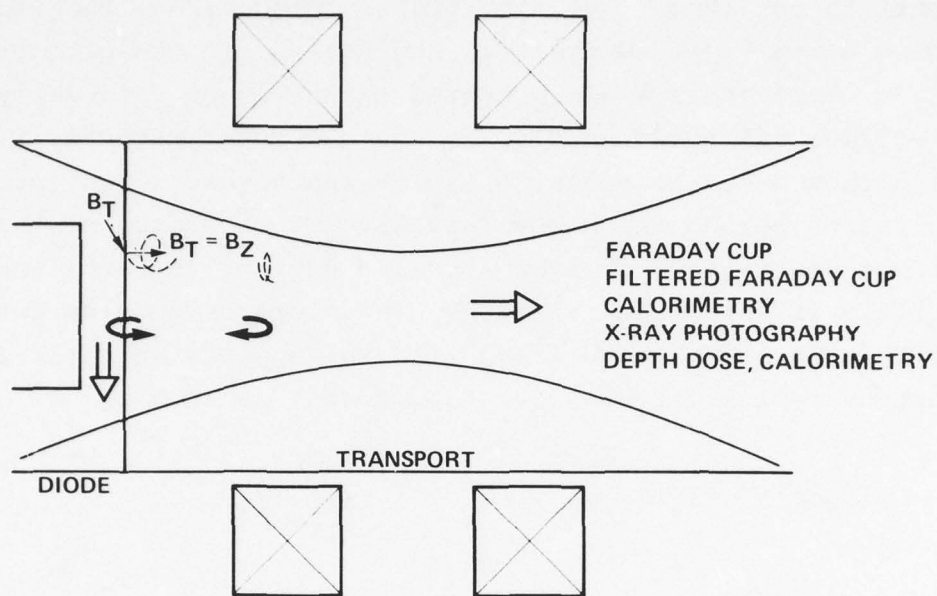
Figure 2.1 Magnetic compression of REB.

9

self-magnetic field (B_θ) of the beam. For the present experimental parameters on OWL II $B \gtrsim B_Z$ and as a result the total magnetic field vector $B_T = B_Z \hat{z} + B_\theta \hat{\theta}$ makes an angle θ_b with respect to normal to the anode. For the present discussion, the radial component of the applied field is neglected. If the Larmor radius of a beam electron is small compared to the anode cathode spacing, the electrons can be assumed to follow the total magnetic field line and thus make the angle, θ_b, with the normal to the anode. In the region beyond the anode (usually 1 torr nitrogen) the beam is current neutralized by plasma return current ($B_\theta \sim 0$) and the total field is normal to the anode. An electron passing through the anode then makes an angle θ_b with the applied magnetic field (neglecting foil scattering for the moment) defined by

$$\theta_b(r) = \tan^{-1} \frac{B_\theta(r)}{B_Z} = \tan^{-1} \frac{I_b(r)}{5rB_Z(r)} \tag{1}$$

where I_b is in kA and B_Z in kG. Here, we assume the field transition at the anode occurs over a distance much less than a Larmor radius. The beam electron angle is thus a function of the radial location of the electron in the beam. This electron angle then increases in the direction of beam propagation as the magnetic field is increased because of adiabatic invariance:

$$\frac{\sin^2 \theta_2}{B_2} = \frac{\sin^2 \theta_1}{B_1} \tag{2}$$

where θ_2, θ_1, B_2, and B_1 are the angle and field at arbitrary positions along the beam. Of course the maximum angle an electron can have and still propagate is 90 degrees. Thus for a given ratio of field between the lens position (maximum field) and diode $M = B_{Z,max}/B_{Z,diode}$, the maximum angle an electron can have

10

at the diode and still pass through the lens is $\theta_m = \sin^{-1}(M^{-1/2})$, the loss cone angle. For our beam and field parameters the angles in the diode substantially exceed θ_m. Thus many electrons will be reflected at some position between the diode and the magnetic field lens. These electrons return to the diode where they are reflected by the applied voltage and returned to the transport region.

We now discuss this process of multiple reflections (shown schematically in Figure 2.1 in more detail). In crossing the anode on their return to the diode, the electrons see an abrupt change in magnetic field direction and undergo an angular scattering. From the scattering process, one obtains a probability that the electron will re-enter the transport region with $\theta < \theta_m$ and be transmitted through the lens. The possible change in θ for a single pass can be assumed to be large, due to the large difference in direction of total magnetic field between diode and transport regions; the probability is thus given by the loss-cone solid angle. Any scattering process in a magnetic field leads to a diffusion across the field lines. Here, the angular scattering at the anode can result in a radial motion of the electrons (inwards or outwards) of up to a Larmor radius at each transit across the anode. Beam transmission through the lens is then determined by that fraction of the beam electrons scattered into $\theta < \theta_m$ before being lost radially out of the beam. This is given by

$$T \cong \left[1 - \frac{\rho_o}{r_c(1-\cos\theta_m)^{1/2}} \right]^2 \qquad (3)$$

where ρ_o is the Larmor radius at the diode [$\rho_o(\text{cm}) = 1.7(\gamma^2-1)^{1/2}/B_T(\text{kG})$] and r_c is the cathode radius. Equation 3 can be compared with the transmitted fraction one would achieve with adiabatic compression only; i.e., no multiple reflections between magnetic

11

field and diode and hence no angular scattering. Again assuming
an angular distribution at the diode given by equation (1),
adiabatic compression would result in

$$T \cong \frac{\theta_m^2 - 0.5\ \theta_s^2}{\theta_b^2} \tag{4}$$

where θ_s is the foil scattering angle. This simplified expression
is valid for our present beam parameters and was obtained by
approximating the results given in Reference 7.

The analysis of Young and Spence actually defines a core
radius for which the beam transmission is given by equation 3.
One has to add a contribution from the adiabatic transmission of
electrons outside this radius. However, for intense beams $B_\theta \gtrsim B_z$
in the diode, the later contribution can be neglected. We will
see that for our present beam parameters, equation 3 predicts sub-
stantially higher transmission than that for simple adiabatic com-
pression given by equation 4.

The increase in beam fluence, namely the ratio of fluence
at the magnetic lens to that at the diode, is given by MT. Using
equation 3 it can be shown that for given diode and beam para-
meters (r_c, I_b, γ) and constant maximum magnetic field B_{max}, there
is a maximum increase in fluence one can achieve by magnetic com-
pression. By taking (MT)/ M = 0 we obtain the magnetic compres-
sion ratio corresponding to maximum fluence increase

$$M = \left(\frac{1}{4\alpha}\right)^{2/3} \tag{5}$$

where $\alpha = 1.7(\gamma^2-1)/r_c B_{z,max}$. Comparison between experiment and
theory for both transmission and fluence as a functio of mirror
ratio is given in Section 4.3.

12

2.2 BEAM ELECTRON ANGLE

Determination of electron beam angle is critical for many material response applications. In this section we discuss several aspects of electron angles in systems involving magnetic compression of intense beams. (Some aspects of electron angle were discussed in the previous section on models for beam transmission.)

It is assumed that an electron emitted from the cathode and crossing the anode for the first time will have an angle as given by equation 1. Since the angle depends on self-magnetic field and hence on current, it is a function of both radius and time. However, for any given radius and time all electrons at the anode have a single angle. This angle then increases as the electron propagates through the converging magnetic field according to equation 2. Equation 1 is in agreement with the trajectory analysis of Forrester (Reference 8). The results of the REEFER computer *diode code* for both circular and rectangular diodes are also in approximate agreement with this model, but show equation 1 slightly over-estimates beam angle. For uniform current density the average angle, averaged over the cross section of the beam, at the anode using equation 1 is then given by

$$\langle\theta\rangle = (1+\alpha^2)[\pi/2 - \tan^{-1}\alpha] - \alpha \qquad (6)$$

where $\alpha = B_z/B_\theta(r_c)$. For intense beams this average angle can be quite large; with the OWL parameters of this program $\langle\theta\rangle \cong 45$ to 50 degrees. Current non-uniformities, radial components of both the applied magnetic field and electric field in the diode, as well as a finite thickness anode plasma, will all complicate this simplified model.

13

However, even without these latter effects, models for electron angles are more complex in the presence of reflected electrons. Now the electron angle is not only determined by the field in the diode but by the scattering process as well because of the abrupt change in magnetic fields encountered at the anode by returning electrons. Rather than a single angle as used in equation 1, one has a distribution of angles that can depend on radius and time. Since the scattering is a stochastic process, the angular distribution is best calculated or modeled using computer codes. This was not done in the present program, but is a subject of a diagnostics program (Reference 9). Here we only consider some aspects of how the distribution of angles evolves as the beam propagates first through the increasing and then through the expanding magnetic field.

First we consider the region between the anode and the magnetic lens. At the anode, only those electrons having angles less than $\theta_m = \sin^{-1}(M^{-1/2})$ need to be considered. If we define $P(\theta)$ as the distribution of angles at the anode, the number of electrons having angles between θ and $\theta + d\theta$ is $P(\theta) 2\pi \sin\theta d\theta$. If we denote θ' as the corresponding angle at the magnetic lens, conservation of particles requires

$$P(\theta) \sin\theta \, d\theta = P(\theta') \sin\theta' \, d\theta' \qquad (7)$$

Since any given electron with angle θ will evolve according to equation 2 in propagating to the lens, the angular distributions are related by

$$P(\theta') = \frac{P(\theta)}{M} \frac{\cos\theta'}{\left(1 - M^{-1} \sin^2\theta'\right)^{1/2}} \qquad (8)$$

where we have used equation 2 to evaluate $d\theta/d\theta'$. Equation 8 is the general transformation law relating angular distributions at

14

the diode and any position in the converging magnetic field. Although the exact form of $P(\theta)$ is not known, some aspects of the distribution at the magnetic lens can be obtained from equation 8. First we consider a uniform distribution of angles between 0 and θ_m at the diode. Evaluating equation 8 one observes that the corresponding angles for this case at the lens are not uniformly distributed between 0 and 90 degrees, but have a maximum in the distribution at an angle somewhat greater than 45 degrees. Because of the stochastic scattering process at the anode, one would expect that $P(\theta)$ is either uniform or slightly peaked near θ_m. The resulting distributions at the lens are similar having a maximum somewhere between 45 and 75 degrees for the parameters of this program.

Of equal importance, for material response applications, is the region beyond the lens, where the beam is expanded. The transformation given by equation 8 applies equally in this region. Although $P(\theta')$ at the magnetic lens is not known at this time, we can still obtain important characteristics of the angular distribution for the expanded beam. If we assume for the moment $P(\theta')$ is uniform between 0 and 90 degrees at the lens then it is easy to compute an average angle for the distribution as the beam expands:

$$\langle\theta\rangle = \frac{\sin\theta_m - \theta_m\cos\theta_m}{1-\cos\theta_m} \tag{9}$$

This is plotted in Figure 2.2 where M is now the ratio of magnetic field at the lens to the value at the expanded position. We note in this figure that the average angle rapidly decreases as the beam expands, which illustrates an important point for material response applications. The process of magnetic compression and expansion of intense beams can be used to "cool" the beam; i.e., reduce the electron angles. For example, if we take the

15

78-8-159
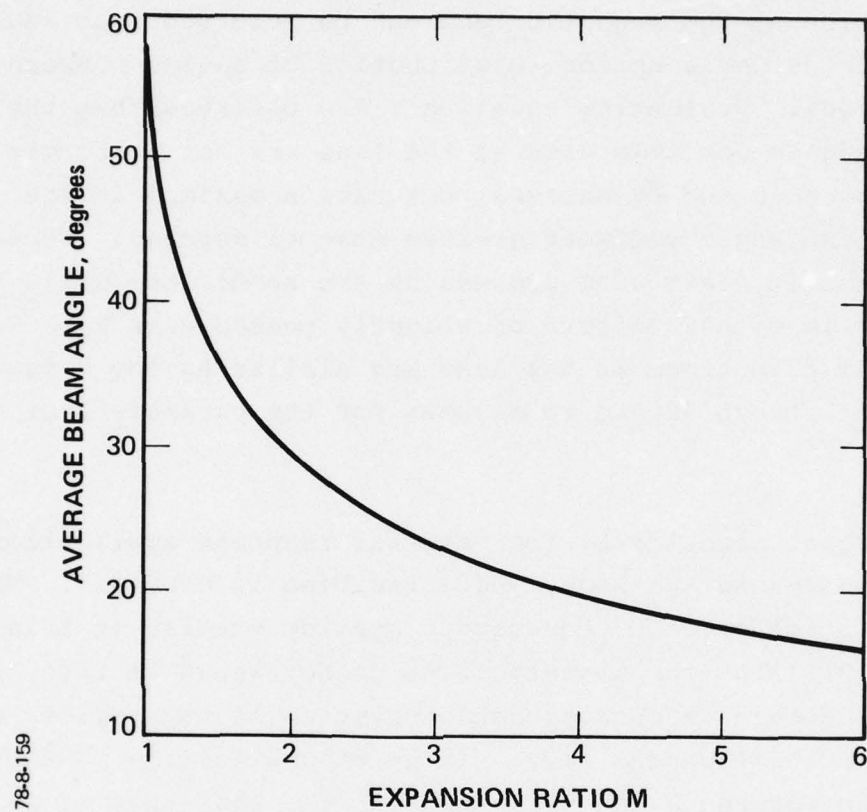
Figure 2.2 Beam electron angle, averaged over the
angular distribution, as a function of
magnetic field expansion ratio.

16

present experimental parameters for OWL (discussed in Sections 4 and 5), we find from equation 6 an average angle at the diode of $\sim$ 50 degrees, whereas with compression and then expansion by M = 3 (i.e., the same fluence position beyond the lens as at the diode) from Figure 2.2, the maximum average angle is $\sim$ 24 degrees. As discussed in the previous paragraph, P(θ') may not be a uniform distribution, but may exhibit a maximum between 45 and 90 degrees, which will make the angles in Figure 2.2 slightly lower.

SECTION 3

APPARATUS

The experimental apparatus used in this program including the OWL II diode, beam transport chamber, magnet coils, and beam diagnostics is shown in Figure 3.1. Several improvements in the diode hardware, beam propagation chamber, and diagnostics were made and tested. Earlier small area beam experiments (discussed in detail in Section 4) were characterized by eratic diode closure and insulator breakdowns. With the improvement in experimental apparatus these two problems, though not eliminated, became less severe (more work in these areas is still required). In this section of the report the changes made resulting in increased performance are discussed, along with recommendations for additional improvements.

An insulator and diode study was conducted on OWL II during September through November 1974 by P. Spence, G. Frazier, and other PI personnel using internal funds. This study first included a series of electrostatic field calculations to define the field grading of the then existing insulator configuration and to determine the effects of tube geometry changes (insulator and electrode feed) on the electric field distribution. With several iterations a tube geometry was found which significantly increased insulator breakdown reliability at high voltage for the large area 400 cm^2 diode (cathode area). The configuration resulted in a lowering of $E_{\parallel}$ at the cathode plate/insulator/vacuum junction (cathode triplepoint) and a lowering of $|E|$ (absolute magnitude) throughout the vacuum region. However, reliability problems still remained on the small area (40 to 80 cm^2) diode configuration for OWL II at high voltage.

18

OUTER TANK WALL
5 ft. DIAMETER

INNER CONDUCTOR
(FINAL TRANSFORMER
SECTION)

ANODE SPACER RING

TO TUBE
VACUUM SYSTEM

SURFACE FLASH-
OVER PREPULSE
SWITCH

DIODE
FILLER
PLATES

FARADAY CUPS,
CALORIMETERS, etc.

ANODE

TO
VACUUM
PUMPS

CATHODE

BEAM
TRANSPORT
CHAMBER

MAGNETIC FIELD COILS

ROGOWSKI COILS

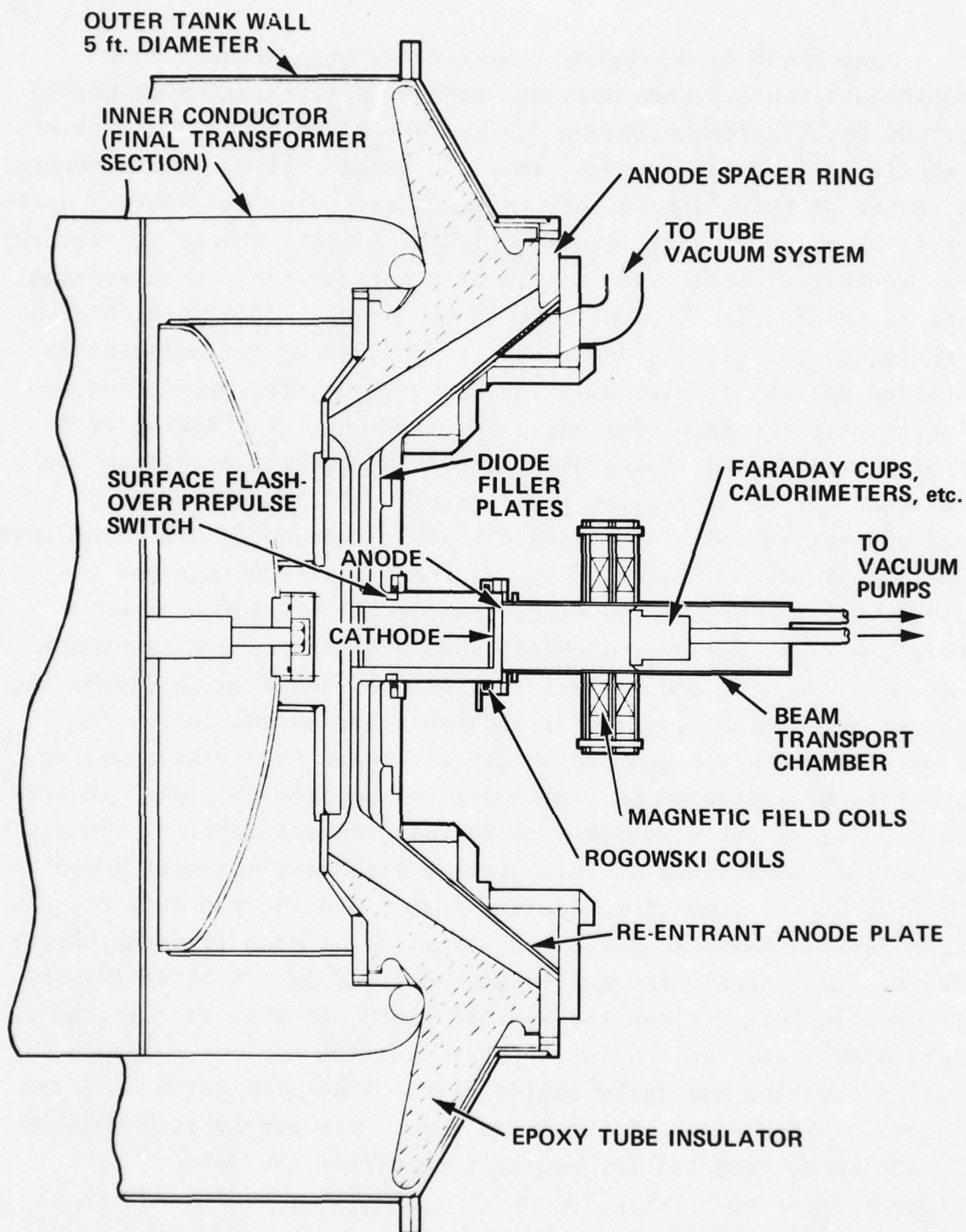RE-ENTRANT ANODE PLATE

EPOXY TUBE INSULATOR

Figure 3.1 OWL II tube, diode, and transport apparatus.

19

Just prior to the present small-area beam program some
additional studies were made on methods of improving performance
of the OWL II diode with the 40- and 80-cm^2 cathode. In initial
calculations it was observed that the small-area diode was nearly
a factor of two higher in vacuum inductance over the 400-cm^2 hard-
ware. For experiments requiring 1.0 to 1.5-MV cathode potentials,
the additional inductive voltage drop resulted in a tube voltage,
and hence electric fields, that exceeded the insulator breakdown
strength. The vacuum inductance was reduced by including anode
"filler plates" (Figure 3.1) and by substantially shortening the
length of the coaxial cathode-anode section. From the electro-
static field plots it was determined that the filler plates could
be added without affecting the electric field at the crucial
cathode triple point, provided the anode cone angle was maintained.
The cathode-anode plate spacing at these filler plates was re-
duced by 2 inches and the resulting electric fields of greater
than 200 kV/cm required magnetic insulation to ensure transport
of energy down to the coaxial section. In addition to shortening
the cathode shank, the radial anode-cathode separation in the
coaxial section was reduced to 2.5 cm, which then also required
some magnetic insulation. Although the applied B_z field can help
to cut off radial electron flow in this coaxial section, the axial
and radial components of this applied field are not well known
because of the various conducting plates and the variable separa-
tion between magnetic coils and diodes to be used in these experi-
ments. In general, the self-magnetic field on the cathode shank
is greater than 5 times the applied field and thus can be used to
determine electrode spacing. Shortening the cathode shank re-
quired removing the large lucite plates that originally provided
vacuum on both sides of the anode cone. The atmospheric pressure
on the anode cone and the higher forces from the magnet coils
produced additional stresses on the anode cone, which had to be
tested. A short series of experiments (1 week on OWL II) on an
IR&D program were conducted to test these diode changes. The

20

initial results were encourgaging and led to the present program
in which successful operation with "filler plates," reduced elec-
trode spacings, shorter coaxial sections, and increased stresses
on the anode cone was verified.

There were several additional modifications made on the
OWL II machine in the present program. A surface flashover pre-
pulse switch was added to the cathode shank to reduce prepulse
affects on the diode impedance for the smaller anode-cathode
spacings required with the 80-cm^2 cathode. Improvements were
made in the beam transport chamber to provide more rapid turn-
around of the beam diagnostics. In addition, a single channel
Faraday cup, a filtered Faraday cup, and segmented calorimeters
were modified for the OWL II beam during initial tests conducted
in this program. These will be discussed in the following sections.

3.1 DIODE DESCRIPTION AND EXPERIMENTAL SETUP

The diode consisted of a 4.0-inch- (10.2 cm) diameter
stainless-steel cathode that was sandblasted after every shot.
The cathode face was either planar or spherically concave with
the depth from center to edge varying from 0.5 to 3.5 mm. To
reduce enhanced electric fields, the edge of the cathode face was
rounded, the radius of curvature varying from 1.6 to 6.4 mm.
The cathode shank was 10.2 cm in diameter, had a 0.10 cm stainless-
steel wall, was polished, and was 30 cm long. The anode cylinder
had an inside diameter of 15.2 cm. For the majority of experi-
ments the anode was 1/2-mil (12.7 microns) titanium stretched
across the anode cylinder. No measurable anode bowing occurred
with titanium for the pressure differentials of 1 torr used in
the experiments. Anode-cathode spacings were varied from 0.7 to
1.5 cm.* During the experiment aluminized mylar anodes (12.7 to

---

*The anode-cathode spacing for the spherical cathodes refer to
 distances from the anode to the cathode edge.

21

25.4 microns thick) were also tested.* Planarity of the anode and
cathode was measured under vacuum and set to plus or minus 0.25 mm
and concentricity of the coaxial anode-cathode section was also
checked and maintained throughout the experiments.

The thickness of the anode spacer ring located at the outer
diameter of the vacuum feed section was reduced from 5.1 cm, as
was used with the large-area diode, to 2.5 cm in order to further
reduce diode inductance. The total thickness of the two anode
filler plates was 5.1 cm, reducing the cathode to anode plate
spacing in this region to 5.3 cm.

The filler plate closest to the cathode plate contains six
monitors: four segmented Rogowski coils 90 degrees apart in
azimuth (to measure uniformity of the radial current feed and to
diagnose the location of any insulator flashes) and two $\dot{B}$ monitors
for inductive voltage correction. Tube voltage was measured by
a capacitive voltage monitor, diode current waveform by a self-
integrating Rogowski coil located in the anode cylinder radially
outward from the A-K, and the cathode potential or diode voltage
waveform by experimentally subtracting from V_T the inductive
voltage drop. This inductive correction was determined on shorted
shots (cathode face shorted to a thick copper anode foil) using
the $\dot{B}$ monitors. The shorted shots were also used to calibrate the
segmented Rogowski coils to the diode current monitor. The result-
ing corrected diode voltages were accurate to $\pm$ 50 kV at peak
voltage.

A surface flashover prepulse switch made of nylon was placed
in the cathode shank. The length of the flashover surface was
varied from 0.5 to 1.5 cm. The outer diameter of this surface

_____

*During vacuum pump down of the system the anode-cathode spacing
 collapses by 0.343 cm due to stress distortion of the radial feed
 section and O-ring compression. The quoted anode-cathode spac-
 ings refer to vacuum conditions.

was 10.0 cm and recessed 1 mm below the surface of the cathode
shank to provide approximate plane-plane surface breakdown. The
switch is located 14 cm from the base of the cathode shank. A
discussion of the prepulse switch including its design criteria
and performance is presented in Section 4.1.

3.2   BEAM TRANSPORT CHAMBERS AND MAGNET COILS

The beam transport chamber first used in this program
consisted of a series of 15.2-cm inside-diameter stainless-steel
chambers of variable length. The total chamber length could be
varied in integral steps by adding or subtracting a number of
chamber sections. The beam diagnostics were mounted at the end
of the total chamber. A variable length system was needed in
order to locate diagnostics either at the maximum magnetic field
position, which varied with respect to the diode, or in the region
of magnetic field expansion. The majority of this hardware had
been built for previous programs.

After the first experiments were conducted, and an approxi-
mate location of the diagnostics was determined, this somewhat
cumbersome vacuum chamber system was replaced by a single stainless-
steel chamber with an inside diameter of 15.2 cm and a 76 cm length.
All diagnostics were modified to slide inside the new chamber,
allowing for a continual change of location. Return current con-
tact between each diagnostic and vacuum chamber wall was provided
by beryllium-copper finger stock. The chamber was filled to a
pressure of 1 torr of nitrogen. Electrical signal connections for
all diagnostics were provided by vacuum feedthroughs at the far
end of the vacuum chamber. The Faraday cups also had an inde-
pendent vacuum system.

Two solenoid magnets were used. These differed only slightly in the magnitude and profile of the applied magnetic field. In each case the fields were measured with the coils mounted on OWL to account for any field distortion from conducting materials. The coils were driven with a 10-kV, 4000-μF, 200 kJ capacitor bank with peak fields varying from 25 to 35 kG with a risetime of 7.5 ms. The solenoid consisted of two 100-turn coils connected in series with a clearance bore of 20.3 cm diameter. A profile of the magnetic field corresponding to 8 kV applied voltage is shown in Figure 3.2. The mid plane between the coils corresponds to the location of peak magnetic fields. The magnitude of beam compression was varied by changing the distance from the diode to the solenoid mid plane. Figure 3.2 shows the location of the diode for a beam area compression of 3.3 to 1.
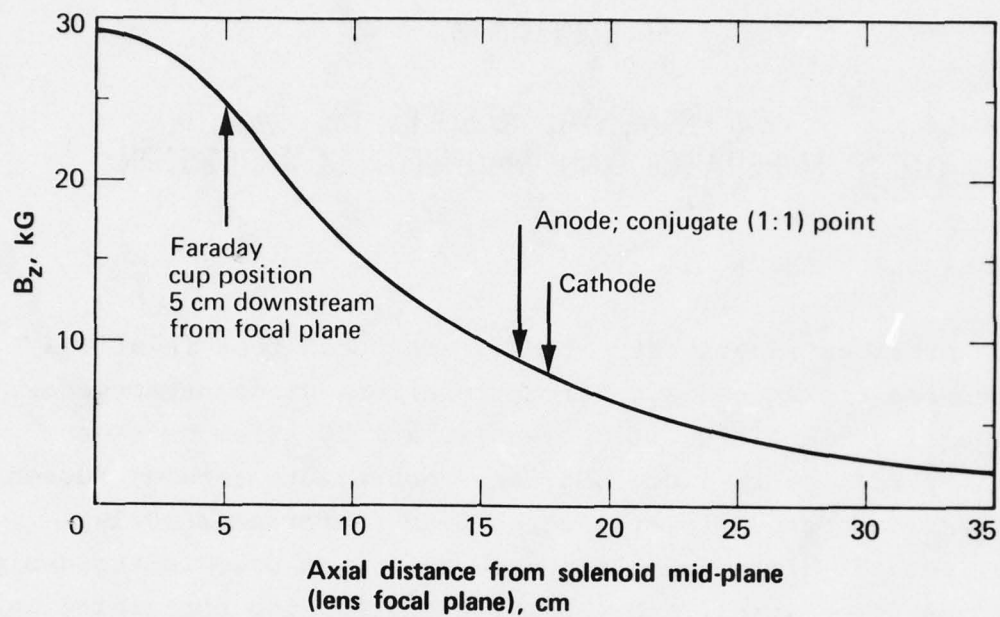
Figure 3.2   Axial profile of the externally
              applied B_z field, measured on-axis.

SECTION 4

EXPERIMENTAL RESULTS ON
DIODE IMPEDANCE AND MAGNETIC COMPRESSION

4.1 PREPULSE EFFECTS

In previous experiments it has been noted that relatively low prepulse fields can significantly affect diode performance. Prepulse electric fields of between 10 and 20 kV/cm have been correlated with early diode shorting, nonuniform cathode turnon, and a resulting nonuniform electron beam (References 10-13). Several methods of reducing prepulse have been used in the design of the generator itself. OWL has a prepulse slab containing an array of eight self-breaking prepulse switches. For a tube voltage in excess of 1.5 MV, the resulting prepulse on OWL II can be about 20 kV, lasting for approximately 1 μs before the arrival of the main pulse. With the 80 cm^2 diode, the required A-K spacings of $\sim$1 cm results in prepulse electric fields in excess of the nominally allowed value of 10 kV/cm.

For the present program a surface flashover switch was placed in a cathode stalk to capacitively divide the prepulse voltage. The equivalent circuit for the vacuum region of the diode is given by

$$V_{diode} = \frac{C_{SW}}{C_L + C_{SW}} V_{PP} \tag{1}$$

where C_{SW} is the switch capacitance, C_L is the load capacitance or capacitance to ground of the cathode from the switch to the A-K region and V_{diode} is the prepulse appearing at the diode for a

26

given prepulse voltage V_{PP} at the tube insulator. From this relationship we see it is important to minimize switch capacitance and maximize C_L by placing the switch as close as possible to the base of the cathode. However, screening of the diode insulator from the ultraviolet radiation occurring during surface breakdown of the switch is essential and determines the switch location. The location and dimensions of the prepulse switch are given in Section 3.2. No direct line of sight existed between the switch and any parts of the tube insulator.

The prepulse switch used in these experiments gave a 4 to 1 reduction in prepulse voltage at the diode. Approximate diode prepulse voltages with the switch installed were measured with a resistive voltage divider across the switch, inside the cathode stalk; the signals were read through the transit-time isolator.

A complete correlation between diode behavior and beam uniformity with prepulse effects was outside the scope of the program. An observation regarding beam uniformity is given in Section 5.1.

It was determined early that overall diode impedance lifetime was increased and the frequency of early shorts reduced with the use of the prepulse switch. It was therefore installed for the remainder of the program, and additional methods were investigated to further improve diode performance. One cm was selected for the length of the flashover surface. It was also found that the prepulse switch had to be replaced after one or two shots. Surface tracking and degradation resulted in erratic diode behavior on subsequent shots with the same switch. Thus although providing increased diode performance this switch has one drawback in that a sufficient number have to be fabricated for replacement after each shot.

A second design in which an inside surface flashover switch was mounted at the cathode base was also tested. However, screening of the tube insulator with this second design was inadequate resulting in frequent tube insulator breakdowns during the main pulse. Recently, a prepulse switch, which also incorporates a hidden inside flashover surface, has been designed and successfully tested in separate programs on the PITHON generator at PI. Although this switch has to be cleaned after each shot, it can be operated for many successive shots (10 to 20), and a similar design could be incorporated into the small-area diode hardware.

4.2 DIODE IMPEDANCE LIFETIME

Impedance collapse has been one of the limiting factors in achieving reliable diode performance at high beam fluence. In the past, however, the relationship between closure velocity and beam parameters has not been well understood. This situation has been caused by several factors: short duration pulses (about 50 ns), the limits of the diagnostics, and the lack of computer data reduction. As a result, the experimenter has been able, at best, to design diode geometries with sufficient margins to avoid catastrophic shorts, a task which became more difficult for beams with larger energy density and longer pulse lengths. The shots on OWL II analyzed in this section were taken using the small-area beam hardware in IR&D experiments just prior to the present contract. However, the results have been verified in each subsequent pulsing session during this program and are the main reason for selecting the 80-cm^2 cathode to develop the small-area beam on OWL II for material response applications.

As a model for relating the time-dependent current and voltage in the diode, we use the planar, nonrelativistic Child-Langmuir relationship with variable spacing and scaling constant:

28

$$I = 2.335 \frac{K A V^{3/2}}{d(t)^2} \qquad (2)$$

where A is in cm^2, d in cm, V in MV and I in kA. The parameter K is an enhancement factor for electron current which can include several effects such as increased emission at the cathode edge, finite aspect ratios, positive ion flow, etc. The major electron (current increase in the present data comes from bipolar flow--the presence of positive ions counterstreaming with the electrons--which, if occurring over the entire beam area, yields a theoretical value of K = 1.86. In addition we consider the dose deposited in the anode:

$$D \ (J/gm) = \int_0^\tau J(t) \ V(t) \ \eta(t) \ dt \qquad (3)$$

where $\eta(t)$ is a coupling coefficient (cm^2/gm). We now use an approximate model for η. It is found that peak front surface dose is closely proportional to $V^{-3/2}$ over the range 0.2 to 1.5 MV. For beam electron angles from 0 to 30 degrees, $\eta \cong 3.0/V^{3/2}$ where V is in MV. Correcting for large angles and reflections in the diode, we use $\eta = 4.5/V^{3/2}$ in this analysis. This value of η is then inserted into Equation (3), and dose versus time is calculated using measured voltage and current waveforms. This relationship for the coupling coefficient is of course very simplified, but it provides for a consistent, uniform treatment of different "shots" relative to each other and gives approximate absolute magnitudes for dose.

In Figure 4.1 we have voltage and current versus time for three shots from computer-generated plots of digitized data. From top to bottom, the traces represent an increase in beam energy density and, hence, anode dose. As the energy density increases, the relative pulse width shortens, but does not influence some parameters such as peak power; it does, however, affect the integrated beam energy ($\int V[t] \ I[t] \ dt$). Little of the physical processes occurring in the diode, which are determined in the analysis of the following paragraphs, are easily discernible from these traces or from impedance plots.
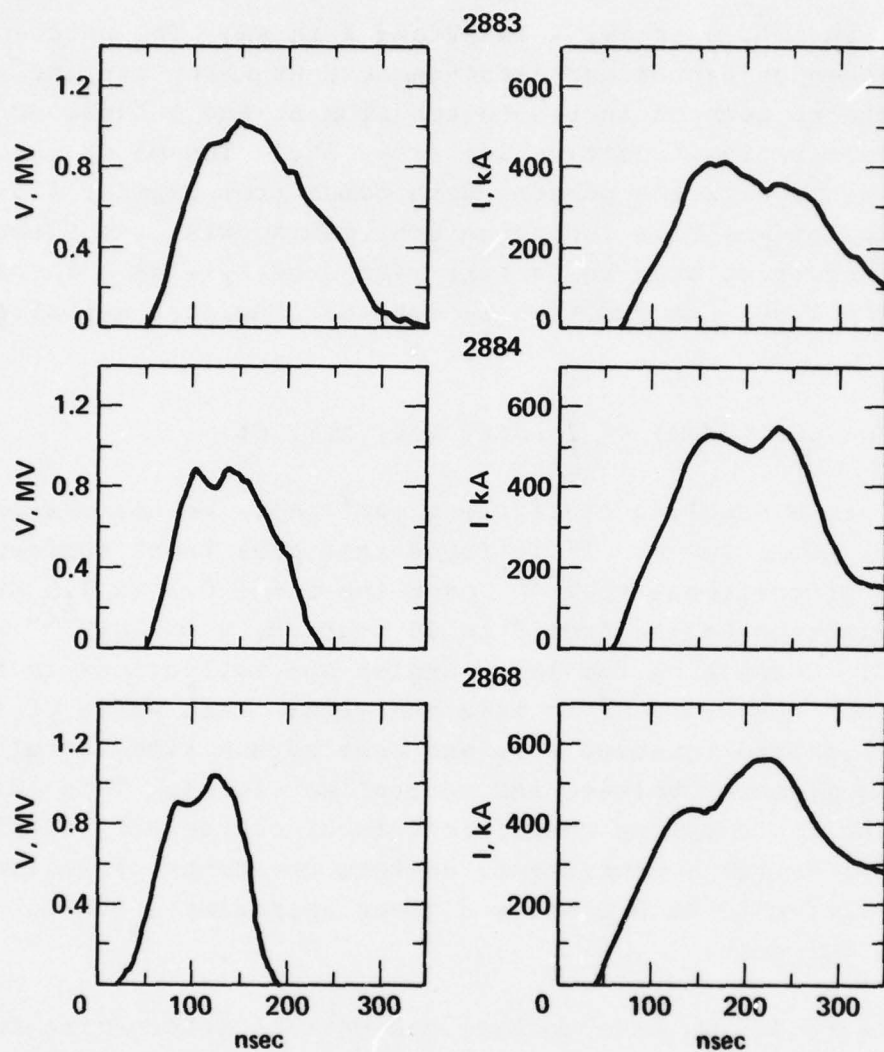
29

Figure 4.1   Voltage and current traces for OWL II
shots 2883, 2884, and 2868.

30

Consider next, Figure 4.2, in which we plot diode current versus the measured inductively corrected voltage for shot 2883. In this shot the 80-cm^2 diode, an initial A-K spacing of 9.3 mm, and a 0.5-mil titanium anode were used. Some other parameters are total beam energy = 50 kJ, $\langle V \rangle$ = 0.8 MV, and $\langle Z \rangle \cong 2$ ohms. Overlayed as dotted lines are Child-Langmuir curves for an A-K (d_o) of 10.0 mm, 9.0 mm, and 9.0 mm with an enhancement K = 1.57, all with no closure. The annotation marks on the I-V curve indicate 5-ns time increments. Calculated anode dose levels at various points are also labeled. We observe that it takes about 175 kV (200 kV/cm) to begin to "light" the cathode as shown by the applied voltage at current onset. The cathodes were planar with a sandblasted stainless steel front surface. The current onset is followed by approximately 10 ns to reach space-charge flow, at which time the diode follows very closely Child-Langmuir behavior corresponding to emission from the entire cathode. The closure velocity in this space-charge phase is very low (< 1.4 cm/μs). At an anode dose of 300 J/g, we observe an increase in current for constant voltage lasting for 25 ns, corresponding to a transition to bipolar flow. The anode plasma formed at this time becomes a source of ions that allows an increase in the electron current. The actual electron current increase in this shot was 1.57. There is then a short period of bipolar space-charge flow followed by rapid A-K closure. The positions marked with letters indicate time intervals over which the gap closure velocities given at the top of the figure were averaged.

Figure 4.3 shows another I-V plot for the same diode (shot 2884, initial A-K, 8.0 mm, E = 45 kJ, $\langle V \rangle$ = 0.75 MV, and $\langle Z \rangle \cong 2$ ohms). This shot exhibits very similar early-time behavior. The dotted lines correspond to Child-Langmuir with d_o = 9.0 mm, d_o = 8.0 mm, and d_o = 8.0 mm with K = 1.86. Assuming the initial closure velocity of 1.5 cm/μs remains constant during the bipolar transition, the actual current increase due to ions is 1.63. The most important fact is that the higher dose rates for this shot cause larger closure velocities after the bipolar transition which, together with the smaller A-K, result in a shorter pulse.
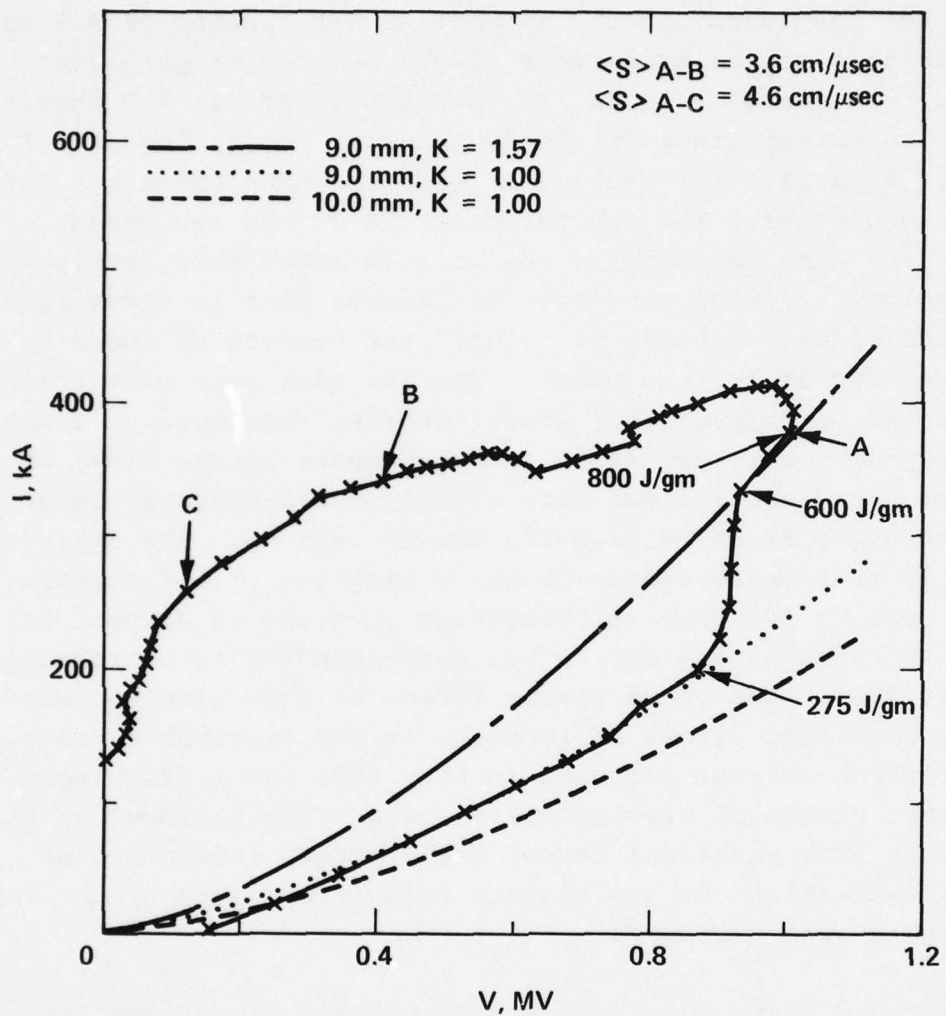
31

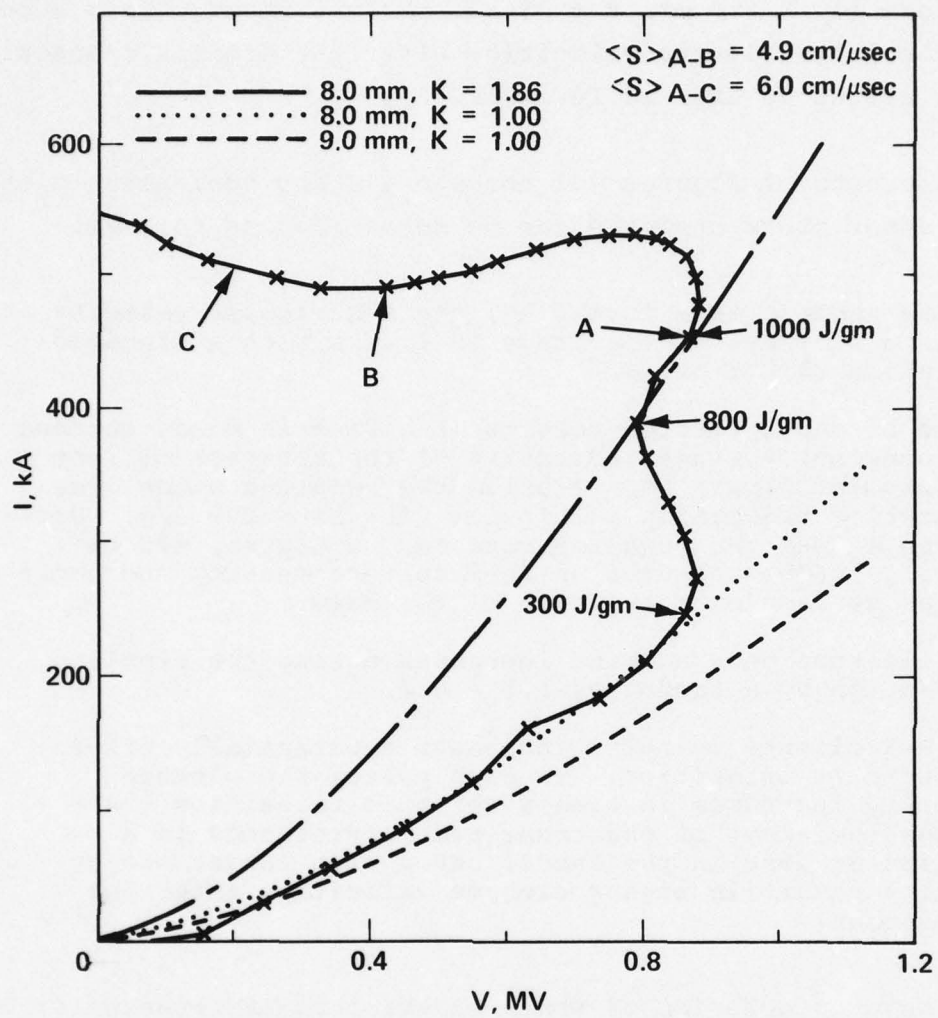Figure 4.2 Diode current versus cathode voltages (shot 2883).

Figure 4.3   Diode current versus cathode voltages (shot 2884).

33

As a comparison we show in Figure 4.4 an I-V plot for the 40-cm^2 diode (d_o = 6.0 mm, E = 35 kJ, $\langle V \rangle$ = 0.85 MV, $\langle Z \rangle \cong$ 3 ohms). We note the large closure velocities after the bipolar transition, achieving values as high as 10 cm/μs.

The results of Figures 4.2 through 4.4 and equivalent plots for many other shots analyzed can be summarized as follows:

- Before anode plasma formation, the A-K closure velocity is 1 to 2 cm/μs. The average is 1.4/μs with a standard deviation of 0.5 cm/μs.

- Anode plasma formation results in a rise in diode current for constant voltage indicative of the presence of ions and bipolar flow. For titanium the required anode dose to start a transition to bipolar flow is $\sim$ 300 J/g. For carbon anodes the required dose may be higher, 400 to 600 J/g. (This assumes uniform current density and hence are an average over the area of the beam.)

- The electron beam current increases during the bipolar transition by a factor of 1.5 $\pm$ 0.2.

- The A-K closure velocity increases substantially after the bipolar transition. In each pulse, the closure velocity increases in time after this transition. Although the start of the transition corresponds to a particular dose in the anode, beams with larger energy density result in higher closure velocities after the transition.

The major conclusion of these experiments (Reference 14) is that very large closure velocities are observed at high beam energy densities, and the onset of these increased closure velocities can be correlated with the onset of ion currents from an anode plasma. This rapid impedance collapse is as yet not well understood. More recent experiments on OWL (Reference 8) have indicated that the shorting mechanism may be a localized phenomenon occurring over areas of a few millimeters in diameter at various locations in the beam, indicative of local instabilities. In other studies, (Reference 15) models have concentrated on shorting mechanisms related to the background gas in the diode. The vacuum in the OWL experiments
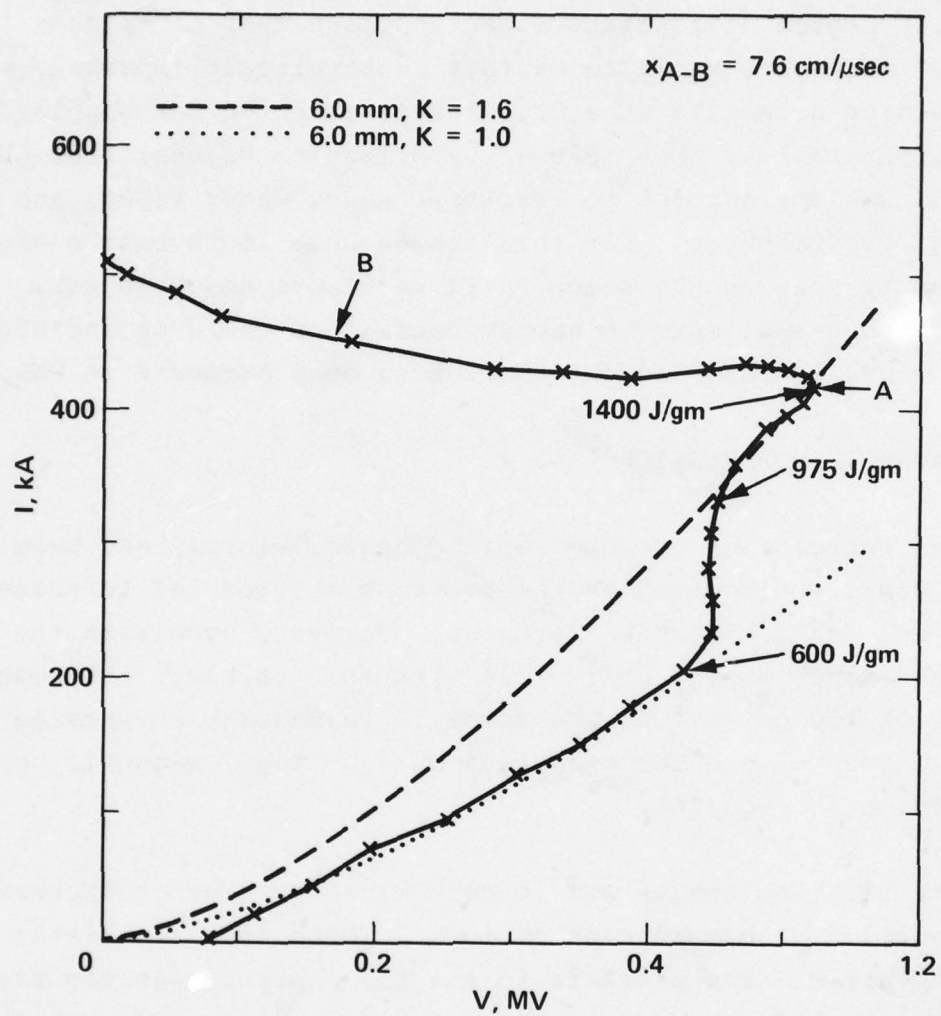
34

Figure 4.4 Diode current versus cathode voltages
(shot 2868).

is typically several times 10^{-5} torr. The ions from the anode plasma can be a very effective means of ionizing this background gas. The degree of ionization can approach that of "plasma filled diodes," which are known to exhibit short circuit impedance phases. It should be noted that the dose levels observed for bipolar transition are less than melt or vaporization values; thus the anode plasma corresponds to absorbed gases, water vapor, and absorbed hydrocarbons. For this reason some improvements might be obtained by heating the anode foils to remove absorbed gas. Both heated anodes and improved vacuum conditions could be included in future experiments using the small-area beam hardware on OWL II.

4.3 MAGNETIC COMPRESSION

The correlation between rapid closure velocity and beam energy density discussed in the previous section led to selecting the 80-cm^2 cathode for this program. However, even with the increased diode energy achievable with this cathode, the beam fluence of 150 cal/cm^2 at the anode is inadequate to provide the required dose of greater than 1500 cal/g. Thus, magnetic beam compression is required.

The first objective was to determine the fluence increase as a function of compression ratio M. There are essentially two ways to vary M. The first is to fix the applied magnetic field in the diode and vary B_{max}. This requires a solenoid containing several coils in which the axial current density can be varied using different parallel/series combinations of individual coils. The second method, which was the one used in this program, varies M by moving a set of magnetic coils relative to the diode with fixed applied voltage to the coils. In this latter method the ratio of applied to self-magnetic field in the diode varies and of course must be included in the models when comparing experiment and theory. Varying the ratio B_θ/B_z also limits the maximum M that can be used for a fixed B_{max} because of beam pinching in the diode.

36

In Figure 4.5 we plot current transmission through the lens
versus compression ratio M. The single channel Faraday cup was
used to measure current transmission and was located 5 cm beyond
the solenoid mid-plane. The voltage applied to the coils was
8 kV, corresponding to ~ 29-kG maximum magnetic field. Also
plotted in Figure 4.5 are the predictions from adiabatic theory and
the model of Young, both using corresponding parameters for OWL
on each shot. These models were discussed in Section 2.1. We
observe the complete failure of adiabatic theory to predict beam
transmission for intense beams. Young's model is closer to the
experimental results predicting the shape of the falloff of
transmission with M but slightly underestimating the magnitude of
the transmission. There are several possibilities to account for
the small remaining discrepancy between theory and experiment.
Young's model assumes that when an electron diffuses outward and
reaches the cathode edge, it is immediately lost, whereas the
electric fields in this region of the diode can still return elec-
trons to the transport region. The model also assumes an abrupt
change in magnetic field at the anode, whereas anode-plasma ef-
fects may make this region more continuous. This means lower
injected electron angles. This latter effect can only be deter-
mined by measuring electron angles at the diode, a measurement
scheduled for followon programs.

In Figure 4.6 we plot the current density increase, MT,
versus compression ratio. Again we observe the substantial im-
provement in predicting experimental results using Young's model
versus adiabatic theory. The position of maximum fluence in-
crease versus M is predicted correctly. One additional observa-
tion in this series of shots led substantial support to Young's
model. For shots at M = 4 and 5 there was considerable damage to
the inside of the anode cylinder radially outward from the A-K
region indicating significant energy flow in this direction. As
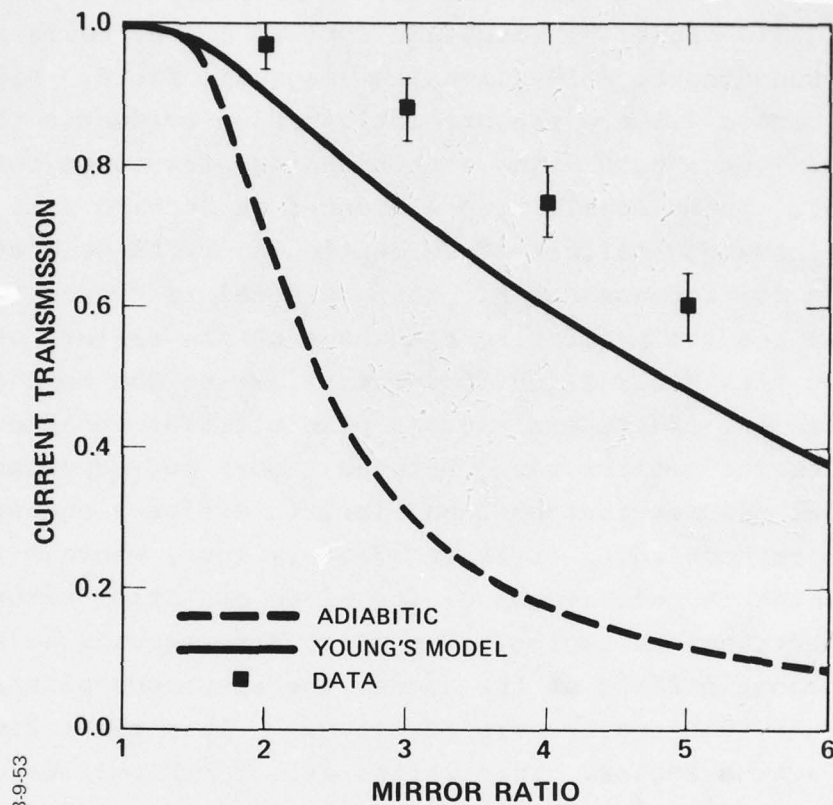stated in Section 2.1, Young's model balances the radial loss of

78-9-53

Figure 4.5   Current transmission through the magnetic
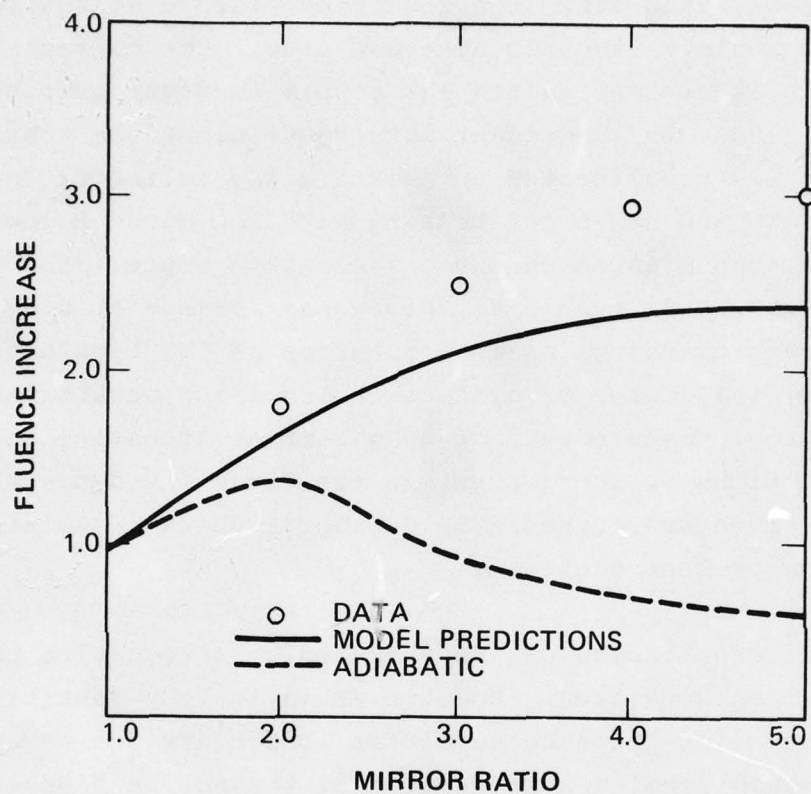field lens as a function of mirror ratio.

38

78-8-161

Figure 4.6   Increase in beam fluence as a function of
compression ratio M.

39

electrons with scattering into angles which can pass through the lens. For the remainder of this program a compression ratio of 3 to 3.3 was used since the resulting fluence at the lens was adequate to achieve required dose and area. The current transmission at peak current (also peak power) averaged over ten shots was 0.85 ± 0.05. On subsequent pulsing sessions the single channel Faraday cup was recalibrated by shorting the collector to the cathode on OWL and cross calibrating with the diode Rogowski coil. The current transmission on three successive shots (3995 through 3997) was 0.93, 0.83, and 0.86, giving an average of 0.87. The actual current transmission is a function of the type of shot; for example, the degree of diode shorting which occurs late in the pulse. Further measurements of beam current transmission including contributions of ion current in the diode and diode shorting effects is given in Reference 9, a program which immediately followed the present contract.

Energy transmission can be measured by integrating the diode and Faraday cup waveforms. However, this is very sensitive to the late-time behavior of these waveforms, which are not as accurate and often would require a truncation of the output signals. Energy transport was measured in this program using a segmented calorimeter (1 inch^2 blocks) located in the expanded region of the beam (expansion ratio $\sim$ 6.5, beam diameter $\sim$ 15.2 cm). For the four shots in which total fluence was measured, latetime insulator flashing reduced the total beam energy to 25 to 35 kJ. On each shot the total fluence from summing calorimeter blocks was compared with the integrated diode energy $\int V_d I_d dt$. The average energy transport (calorimeter energy/integrated diode energy) was 0.82 with a standard deviation of 0.03.

SECTION 5

MEASUREMENTS OF BEAM UNIFORMITY AND ELECTRON ANGLE

5.1 BEAM UNIFORMITY

Beam area, fluence, and uniformity were measured using an
X-ray pinhole camera and segmented calorimeters. One of the first
objectives was to verify that the beam area varied as the ratio of
applied magnetic fields. Some earlier experiments (Reference 5)
indicated that magnetic compression of intense beams resulted in
a "halo" effect (i.e., fractions of the beam outside an area given
by the cathode area divided by the compression ratio). Because of
the fluence levels involved an X-ray pinhole photograph of a tanta-
lum converter was the only method that could be used for obtaining
spatial data at the position of maximum magnetic field. The camera
used in the program was free of "shine through", even for greater
than 50 kJ of 1.5-MV-peak bremsstrahlung radiation. The camera is
used with either a 10 or 20 mil aperture. Figure 5.1 shows pinhole
photographs taken during the first pulsing session for compression
ratios of 3 and 4. In the lower two photographs a lead plate with
"notches" 3.0 cm apart was placed in the converter plane for spa-
tial calibration. We first observed that the beam area compresses
very accurately according to the ratio of magnetic fields. The
film pack used was comprised of a series of X-ray films and fluo-
rescence enhancers yielding a wide dynamic range of sensitivities
for each shot. The edge of the beam was relatively sharp with no
observable radiation outside an area that corresponded to the
cathode area divided by the compression ratio. For the higher

41
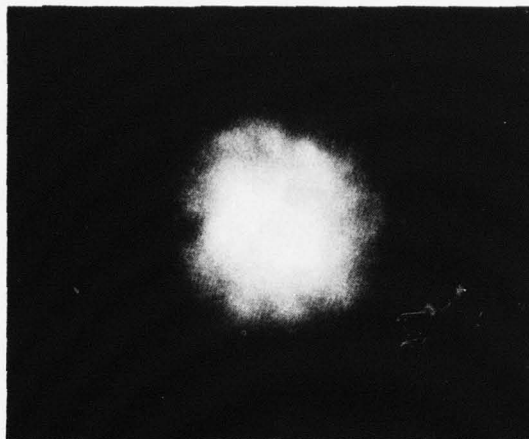
Pulse 3432
M = 3

Pulse 3433
M = 4
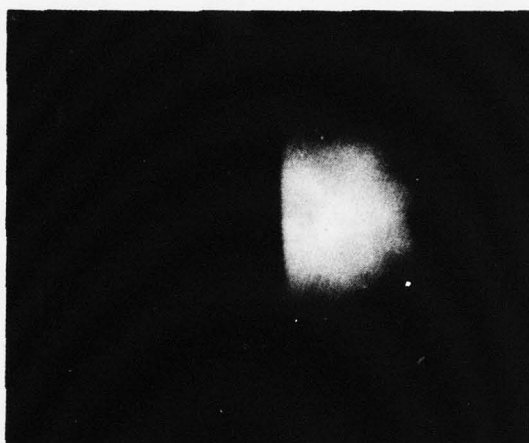
Pulse 3434
M = 3

Figure 5.1   X-Ray pinhole photographs of the beam at the
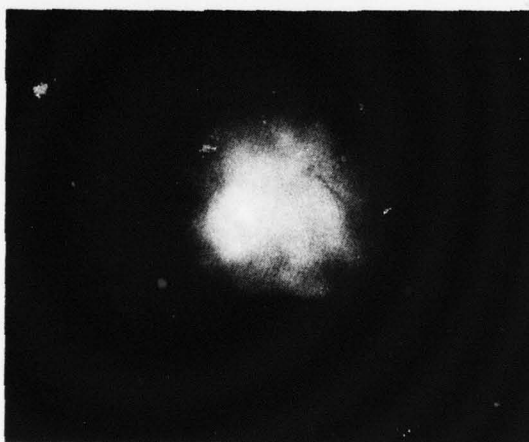   magnetic lens for compression ratios of 3 and 4.

compression ratio, M = 4 and 5, the outer edge of the beam appeared irregular, indicating surface "flute" instabilities. This irregularity was observed both in the photograph and on the graphite collectors for the single channel faraday cup and was also another reason for selecting M = 3 for the remainder of the program. Figure 5.2 shows two additional pinhole photographs taken during the last pulsing session. It was observed both with the pinhole camera and segmented calorimeter that on shots in which the prepulse switch did not hold (thus resulting in either early shorts or insulator flashes from the UV occurring during the prepulse phase) that the beam was often irregular and very nonuniform. A sample is shown in Figure 5.2a.

As shown in Figure 5.2b there is a slight maximum or "hot spot" in the center of the beam. This is typical of cathodes in B_z applied fields. The lower self-magnetic fields on the axis of these diodes are thought to result in shorter total trajectory length for the electrons, lower space charge, and hence increased current density. To minimize this "hot spot" several spherically dished cathodes were tested with qualitative performance observed using the X-ray pinhole photographs. Subsequent shots using segmented calorimeters as a diagnostic and concave cathodes with up to 3.5 mm depth from edge to cathode center indicated optimum performance with 0.75 mm to 1.5 mm depths. Both 2.5 mm and 3.5 mm "dished" cathodes indicated sharp annuli at the outer edge.

By using the wide dynamic range film pack it is possible to obtain film exposures that are in the useful range on the D-logE curve and, hence, that can provide quantitative data on X-ray spatial information. However, this process together with the computer codes required to determine electron to bremsstrahlung conversion are cumbersome and were not used in this program to

43

(a)
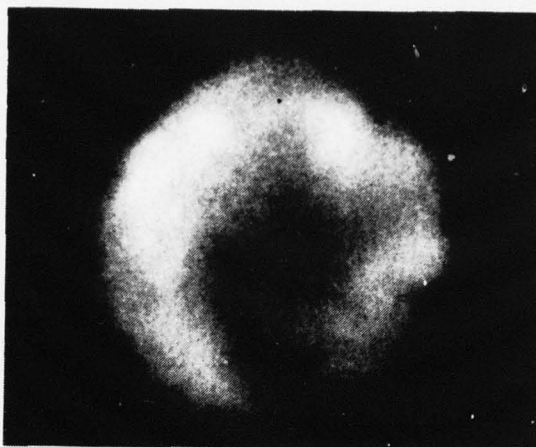
(b)

Figure 5.2   X-Ray pinhole photographs of the beam;
              (a) early short due to prepulse switch
              breakdown, (b) concave cathode with 1.5 mm
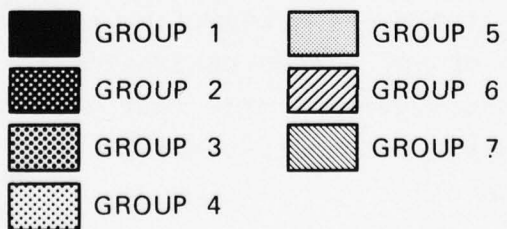   depth from center to edge.

44
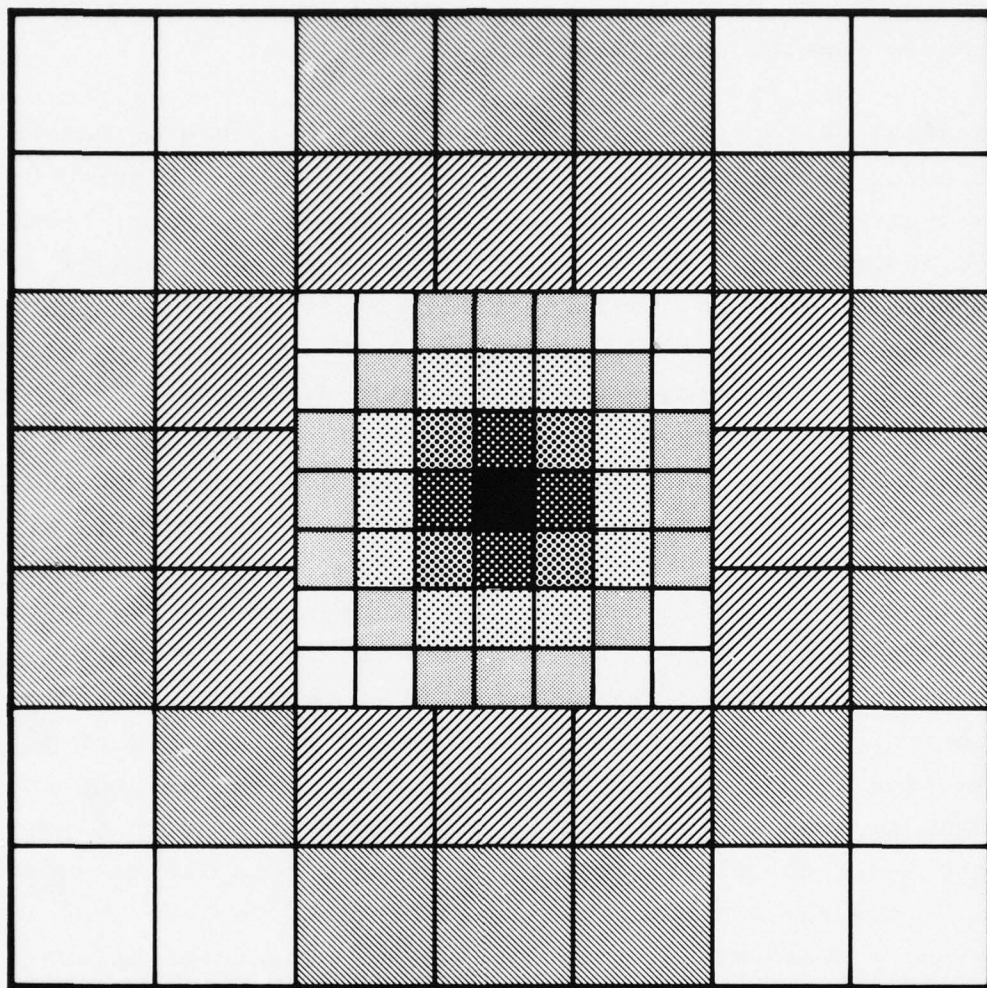
Figure 5.3 Small block segmented calorimeter. Smaller
            blocks are 0.5 cm X 0.5 cm and larger blocks
            are 1 cm X 1 cm.

45

determine beam fluence uniformity. The pinhole photographs were
used, however, to provide qualitative beam cross-section data and
large-scale spatial uniformity.

Spatial uniformity of beam fluence was measured using seg-
mented calorimetry. In the first pulsing session, an array of
2.5-cm-square graphite blocks were used to measure total beam
fluence and indicate fluence uniformity. These were placed in
the expanded region of the magnetic field and energy transport
efficiencies were measured. These measurements were presented in
Section 4.3. In subsequent pulsing sessions, an array of 0.5-cm
and 1.0-cm-square graphite blocks 1.2-cm stick were used.
Figure 5.3 shows the calorimeter configuration along with the
grouping made to determine average fluence versus radius. A
total of one hundred data channels were used. Because of dose
limitations this calorimeter was also located in the region of
an expanded beam. Figures 5.4 to 5.5 show the calorimeter
readings for two shots 4016 and 4023 taken during the third puls-
ing session. In both shots the calorimeter was located at a
position for which the beam area was 1.2 times the cathode area.
The blank squares indicate faulty data channels. At this posi-
tion the small calorimeter blocks correspond to a 2.6 mm square
region at the maximum magnetic field location. We are thus look-
ing for very small scale non-uniformities. The total calori-
meter is measuring the central 35 percent of the beam area. Fig-
ures 5.6 and 5.7 plot average beam fluence (averaged over all
blocks in a given group) versus radius for the same two shots.
From this calorimeter data we note that the "hot spot" which occurs
on the pinhole photograph corresponds to less than 10 percent
increase in fluence.

Central fine-grid readings:

109.6	116.3	123.5	120.3	113.7		113.8
104.3	107.1	114.5	105.6	108.6	93.8	108.3
102.7	107.3	107.9		107.2	100.0	92.9
	92.5	99.3	99.4	110.0	106.7	115.0
98.2	100.2		99.8	103.2	106.0	111.2
87.3	98.2	98.8	97.6	100.1	105.7	104.9
91.0	91.2	97.1	99.7	102.5	97.2	102.9

Outer grid readings:

	108.9		97.6	82.2	118.0	119.0
101.6	102.1	95.4		84.1	106.1	105.0
72.6	68.9				118.0	
83.0						100.2
74.9	89.0				100.3	88.2
77.2	76.5	83.2		90.6	92.3	104.2
73.4	82.0	88.3	85.0	93.9	106.9	93.9

Figure 5.4   Segmented calorimeter readings in cal/cm^2 for shot No. 4016.

Segmented calorimeter grid (outer cells):

	72.2		66.0		82.2	78.3
72.0	67.3	61.8		69.7	73.4	80.0
52.7	69.5				77.3	
76.8	79.1					73.3
	70.6				74.1	73.4
	70.2	71.4		70.1	64.9	77.5
85.4	74.9	66.9	66.6	73.4	62.0	81.8

Central fine grid:

74.7		87.6	86.2	83.3	79.1	88.7
	81.4	91.6	88.1	87.5	83.7	92.8
71.3	74.3	81.9	84.1	89.6		
81.7	75.0	75.5	78.1	70.4	69.9	76.5
	77.6	77.2	89.1	62.4	74.8	83.2
65.7	70.7	76.2	79.8	74.5	81.5	81.5
64.7	70.0	71.5	74.1	78.1		77.5

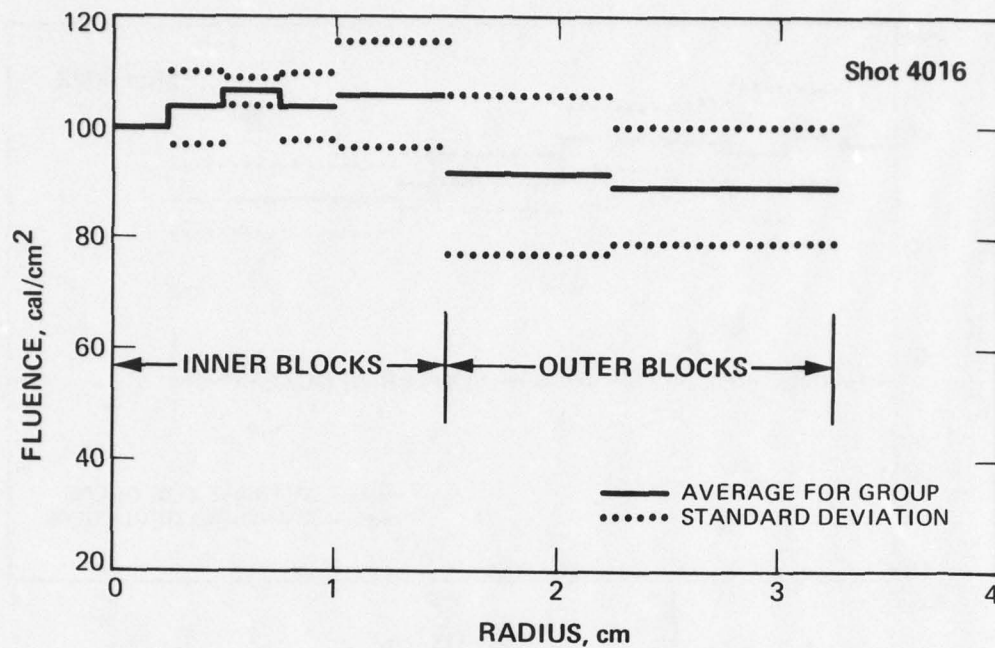Figure 5.5   Segmented calorimeter readings in cal/cm^2 for shot No. 4023.

Figure 5.6 Beam fluence averaged over all blocks in a
          group versus an effective radius for the
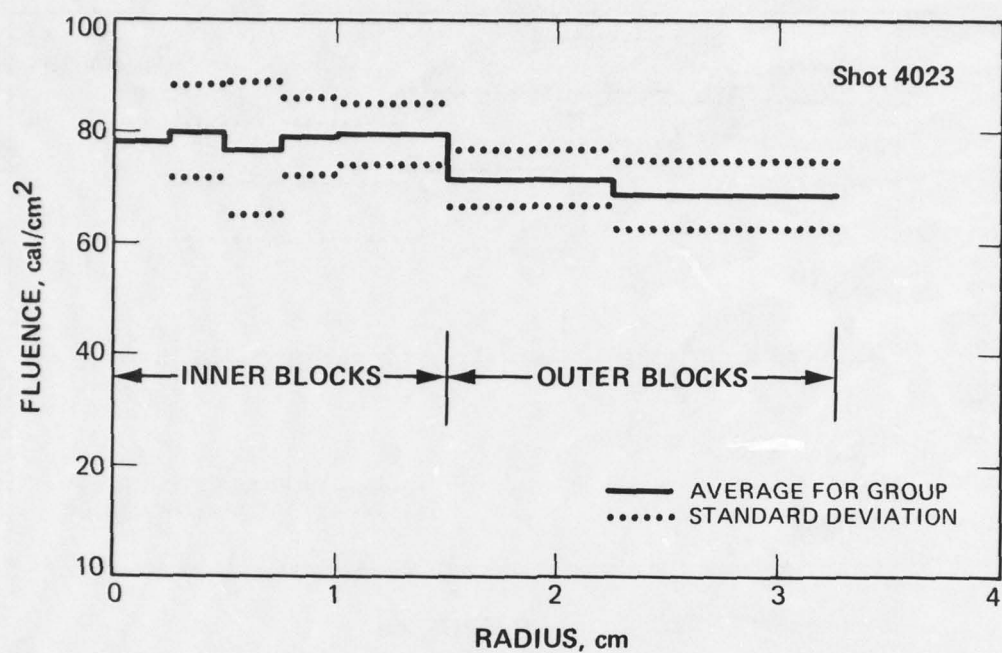   group (shot #4016).

49

Figure 5.7 Beam fluence averaged over all blocks in a
group versus an effective radius for the
group (shot #4023).

50

We can also compare measured fluence at the calorimeter with a value one would calculate for this location using integrated diode energy. Table 5.1 gives the results for four shots. The calculated values assume a uniform beam, 81.2 cm^2 cathode, 0.82 for energy transport, and use 0.83 to correct for beam expansion to the calorimeter location. This table indicates the accuracy to which one can predict fluence at a sample location, at least in the expanded beam region, using diode energy.

5.2 DEPOSITION PROFILES AND BEAM ELECTRON ANGLES

In Section 2.3 we discussed several aspects of the angular distribution for magnetically compressed and expanded electron beams. Although this is a complex subject, there has been significant progress both in our understanding of, and our ability to measure, electron angles for intense beams. The primary objective of this present program was to develop the capability to achieve specified high dose levels. However, several diagnostics were modified and tested in this environment. Already discussed were the single channel Faraday cup, X-ray pinhole camera, and segmented calorimeters. In addition measurements were made with a depth-dose foil calorimeter stack and initial measurements with the time-dependent filtered Faraday cup.

Figure 5.8 shows a measured deposition profile using the foil calorimeter for shot 3457 (E_B = 55 kJ, <V> = .93 MV) The depth-dose calorimeter consisted of ten 20 mil graphite foils. The beam was expanded by $\sim$ 5 at the foil stack location, area 135 cm^2. Using the diode voltage and current waveforms a 1-D Monte Carlo code was used to predict deposition profile. Assuming a single beam angle the resulting calculator profiles for 10° and 20° were also shown in Figure 5.8. The measurements are in agreement with the angle of 15 degrees one calculates at this

51

TABLE 5.1

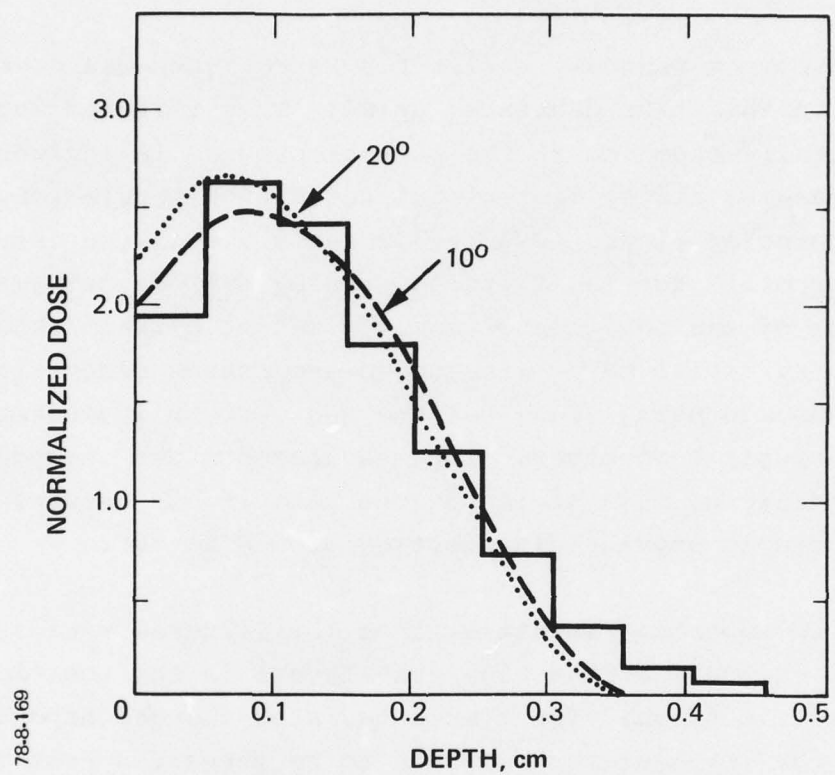| Shot Number	Diode Energy (kJ)	Calculated Average Fluence$_2$ (cal/cm^2)	Measured Average Fluence$_2$ (cal/cm^2)
4016	58.2	117	104
4023	44.9	90	79
4012	57.0	115	112
4024	46.0	92	86

78-8-169

Figure 5.8   Deposition profile from stacked foil calorimeter
located in the expanded beam region.

location using Figure 2.2 from Section 2.3. For diode energies
of 50 kJ or more this is approximately the maximum fluence loca-
tion in which the foil calorimeter can be utilized.

In a previous program, a filtered Faraday cup was developed
and tested on the CAMEL generator at PI. This filtered Faraday
cup was slightly modified in the present program to include a
collector backing plate, increased interchannel insulation, and
graphite protector rings. Figure 5.9 shows a measured charge
deposition profile for the filtered Faraday cup located just
5 cm in back of the position of maximum magnetic field (shot 3459,
E_B = 51 kJ, $\langle V \rangle$ = 1.1 MV). Also shown are charge deposition
profiles computed using diode voltage and current waveforms again
assuming a single beam angle. The measurements are in good agree-
ment with predicted mean angles at the lens if one assumes a
uniform isotropic angular distribution from 0 to 90°.

The most important result is that the filtered Faraday cup
can be used reliably at the high dose levels in the position of
maximum magnetic field. The time-integrated charged deposition
profile is the simplest form of data to be extracted from this
diagnostics. Immediately following the last pulsing session of
this program the filtered Faraday cup was tested and subsequently
analyzed in more detail for time-dependent angular distribu-
tions (Reference 9).

One can obtain an initial estimate of dose versus area for
the small area beam system. Assuming M = 3, E_B = 50 kJ, and an
energy transport efficiency of 0.82 from measurements, we take
a deposition profile in carbon from Monte Carlo runs for a typical
shot with mean voltage of 1 MV, and use the average angle versus

54
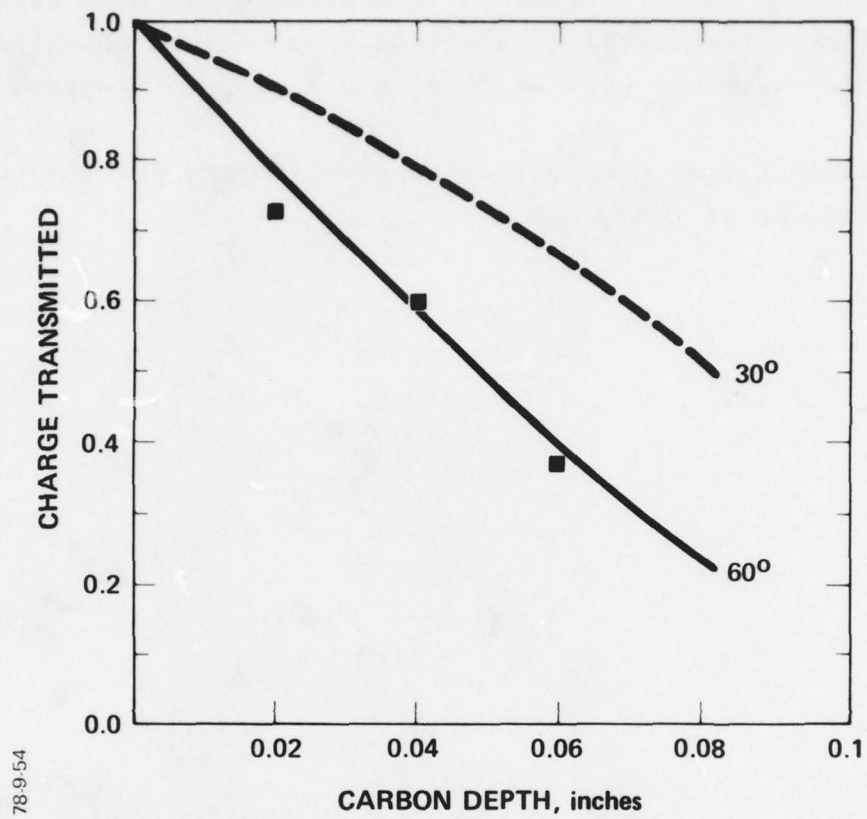
Figure 5.9 Charge deposition profile for shot #3459 using
          the filtered faraday cup near the position of
          maximum field.

55

expansion ratio calculated in Figure 2.2. The results are given in Figure 5.10. A more detailed determination of dose versus area requires measurement of electron angle versus position in the expanded beam and will be made in a follow-on program.

In Table 5.2 we give a reduced shot summary for the third pulsing session of the program.

Figure 5.10   Fluence and peak dose versus area
in the expanded beam (assuming 60 kJ
in the diode).

57

78-8-170

TABLE 5.2

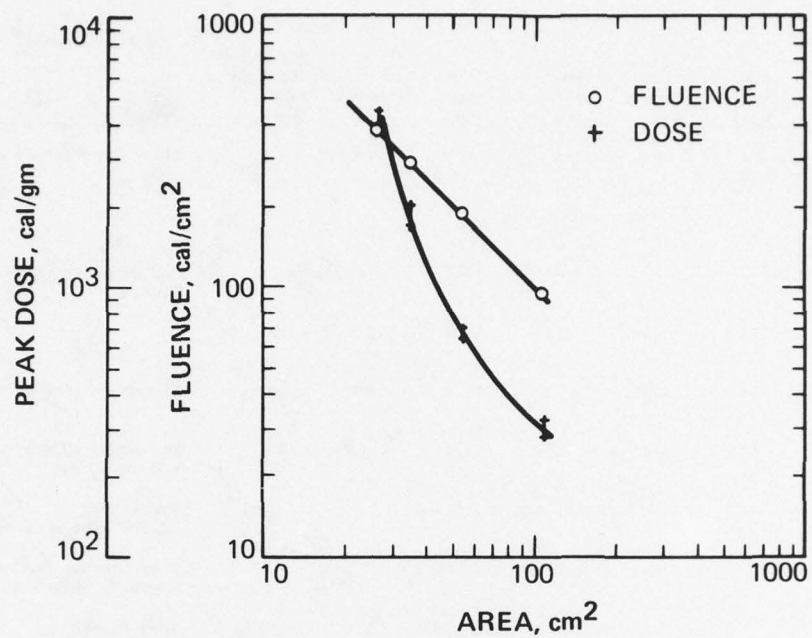| Pulse No.	Type of Pulse	Diode Energy (kJ)	Peak Current (MA)	Peak Voltage (MV)	A-K Gap (mm)	Mean Voltage (keV)	Pulse Width (ns) FWHM Power	Comment
3986	Shorted shot	--	--	--	0	--	--	All mirror ratios are 3:1
3987-3993	Shorted shot	--	--	--	0	--	--	
3994	Faraday cup	--	--	--	11.0	--	--	Bad scope trigger, didn't get signal
3995	Faraday cup	76	0.44	1.63	11.0	~1000	~200	
3996	Faraday cup	55	0.33	1.33	11.0	~800	~140	Second shot on pp switch
3997	Faraday cup	60	0.42	1.30	11.0	~900	~140	New prepulse switch installed for this shot
3998	Faraday cup			Traces not digitized				Tube flash Second shot on prepulse switch
3999	Faraday cup			Traces not digitized				Tube flash Prepulse switch at base of cathode
4000	Faraday cup			Traces not digitized				Tube flash Prepulse switch at base of cathode
4001	Faraday cup	73	0.38	1.65	11.0	~970	~150	Return to pp switch in cathode stalk
4002	Pinhole camera	36	0.45	1.70	11.0	--	~95	Tube flash Prepulse switch at base of cathode
4003	Calorimeter shot	27	--	--	11.0	--	--	Tube flash Prepulse switch at base of cathode
4004	Calorimeter shot	--	--	--	11.0	--	--	Tube flash Prepulse switch at base of cathode
4005	Calorimeter shot	43	0.58	1.30	11.0	~850	--	Return to pp switch in cathode stalk for this and all remaining shots
4006	Pinhole camera	51	0.41	1.52	12.0	~1050	--	Flat cathode 10 mil hole camera 34.5 inches from anode

TABLE 5.2 (cont.)

Pulse No.	Type of Pulse	Diode Energy (kJ)	Peak Current (MA)	Peak Voltage (MV)	A-K Gap (mm)	Mean Voltage (keV)	Pulse Width (ns) FWHM Power	Comment
4007	Depth Dose shot	52.2	0.28	1.40	11.0	~950	195	First 4 to 5 foils spalled. Back to 1.5 mm dished cathode
4008	Filtered Faraday cup	47.4	0.27	1.45	11.0	~850	150	
4009	Filtered Faraday cup	49.4	0.27	1.30	11.0	~900	160	0.75 mm dished cathode
40,10	Depth Dose shot	--	0.28	1.65	11.0	--	160	Flash
4011	Pinhole camera	53.5	0.32	1.25	11.0	~900	195	0.5 mm dished cathode
4012	Calorimeter shot	57.0	0.29	1.60	11.0	~1150	160	
4013	Pinhole camera	60.3	0.36	1.35	11.0	~950	150	0.75 mm dished cathode
4014	Pinhole camera	--	0.29	1.82	11.0	--	--	Flash - Scattering foil - Kapton
4015	Filtered Faraday cup	24.0	0.25	1.50	11.0	~1200	115	Flash
4016	Calorimeter shot	58.2	0.31	1.40	10.0	~1050	195	
4017	Calorimeter shot	--	0.21	1.85	10.0	--	--	Flash, 1.5 mm dished cathode
4018	Filtered Faraday cup	63.5	0.42	1.35	10.0	~900	160	0.75 mm dished cathode
4019	Filtered Faraday cup	44.0	0.32	1.40	10.0	~1150	155	
4020	Filtered Faraday cup	53.2	0.30	1.40	10.0	~1200	190	
4021	Filtered Faraday cup	48.0	0.32	1.46	10.0	~1200	150	
4022	Filtered Faraday cup	55.2	0.45	1.35	10.0	~930	155	0.75 mm dished cathode
4023	Calorimeter shot	44.9	0.28	1.51	10.0	~1200	160	
4024	Calorimeter shot	46.0	0.39	1.65	10.0	~1300	155	1.5 mm dished cathode

REFERENCES

1. P. E. Bolduc and E. L. Patterson, J. Appl. Phys. $\underline{43}$, 4006 (1972).

2. J. R. Freeman and J. W. Poukey, J. Appl. Phys. $\underline{43}$, 4010 (1972).

3. H. Davitian and J. Nation, Compression of Intense Relativistic Electron Beams, Cornell University Report, May (1973).

4. P. Spence and K. Nielsen, "DNA OWL II Generator Beam Development Studies," PIFR-665, Physics International Company, San Leandro, CA., (1975).

5. C. Stallings, J. Benford, and K. Childers, Plasma Phys. $\underline{18}$, 317 (1976).

6. D. A. Phelps, J. R. Oldenettel, P. Korn, J. Shannon, App. Phys. Lett. $\underline{29}$, 335 (1976).

7. T.S.T. Young and P. Spence, App. Phys. Lett., $\underline{29}$, 464 (1976).

8. D. W. Forster, "High Current Electron Beam Acceleration in the Presence of an External Magnetic Field: Field Magnitude Criteria," AWRE Note SSWA/DWF/742/648, 1974 (unpublished).

9. B. Ecker, et al., "Intense Electron Beam Generation and Compression: Advances in High Dose Diagnostics and Theory," Physics International Company, PIFR-1045, 1978 (unpublished).

10. R. D. Genuario and K. Triebes, "Intense Relativistic Electron Beam Focusing Experiments," IEEE Conference Record Abstracts, 1976, IEEE International Conference on Plasma Science, No. 76CH 1083-5-NPS, 1976.

11. T. G. Kelley and R. L. Schuck, "Transmission and Compression of an Intense Relativistic Electron Beam Produced by a Converging Annular Diode with Return Current Feedback Through the Cathode," Sandia Laboratory, Albuquerque, Internal Report No. SAND-75-0668, 1976.

REFERENCES (cont.)

12. P. D.'A. Champney and P. W. Spence, "X-Ray Source Size Pro-
    duction of a 2 Terrawatt Pulsed Electron Radiographic Ac-
    cellerator," Physics International Internal Report PIFR-932,
    1977.

13. P. D.'A. Champney et al., "Vacuum Switch for High Repetition
    Rate Accelerator Applications," Physics International,
    PIP-1783, 1978.

14. D. R. Dakin and J. Benford, "Closure Velocity in B_z Diodes,"
    Bulletin of IEEE Conference on Plasma Science, Troy, N.Y.,
    May 1977.

15. J. M. Creedon, "Ionization of the Background Gas and the
    Voltage Collapse Phenomena in the High ν/γ Diodes," Physics
    International Technical Note 8400-01, 1978.

DISTRIBUTION LIST

DEPARTMENT OF DEFENSE

Assistant to the Secretary of Defense
Atomic Energy
    ATTN: Executive Assistant

Defense Documentation Center
12 cy ATTN: DD

Defense Intelligence Agency
    ATTN: DT-1B, R. Rubenstein

Defense Nuclear Agency
    ATTN: RAEV
    ATTN: DDST
    ATTN: STVL
4 cy ATTN: TITL

Field Command,
Defense Nuclear Agency
    ATTN: FCPR

Field Command
Defense Nuclear Agency
Livermore Division
    ATTN: FCPRL

Joint Strat. Tgt. Planning Staff
    ATTN: JSAS

Under Secretary of Defense for Rsch. & Engrg.
    ATTN: Strategic & Space Systems (OS)

DEPARTMENT OF THE ARMY

Deputy Chief of Staff for Rsch. Dev. & Acq.
Department of the Army
    ATTN: DAMA-CSS-N

Harry Diamond Laboratories
Department of the Army
    ATTN: DELHD-N-RBA, J. Rosado
    ATTN: DELHD-I-TL
    ATTN: DELHD-N-NP
    ATTN: DELHD-N-RB-I, P. Caldwell

U.S. Army Missile R&D Command
3 cy ATTN: RSIC
    ATTN: DRCPM-PE-EA

U.S. Army Nuclear & Chemical Agency
    ATTN: Library

U.S. Army Test and Evaluation Command
    ATTN: DRSTE-EL

DEPARTMENT OF THE NAVY

Naval Intelligence Support Center
    ATTN: NISC-45

Naval Research Laboratory
    ATTN: Code 6701, J. Brown
    ATTN: Code 6707, J. Davis
    ATTN: Code 7770, G. Cooperstein

DEPARTMENT OF THE NAVY (Continued)

Naval Weapons Center
    ATTN: Code 233

Office of the Chief of Naval Operations
    ATTN: R. Blaise

Naval Surface Weapons Center
White Oak Laboratory
    ATTN: Code F31
    ATTN: Code R40

DEPARTMENT OF THE AIR FORCE

Air Force Weapons Laboratory
    ATTN: NT
    ATTN: CA
    ATTN: DYP
    ATTN: SUL
    ATTN: DYC

Deputy Chief of Staff
Research, Development & Acq.
Department of the Air Force
    ATTN: AFRDQSM

Space and Missile Systems Organization
Air Force Systems Command
    ATTN: DYS

Space and Missile Systems Organization
Air Force Systems Command
    ATTN: IND, D. Muskin

Space and Missile Systems Organization
Air Force Systems Command
    ATTN: MNNH

Space and Missile Systems Organization
Air Force Systems Command
    ATTN: SKF, P. Stadler

DEPARTMENT OF ENERGY CONTRACTORS

Lawrence Livermore Laboratory
University of California
    ATTN: L-153
    ATTN: L-545
    ATTN: L-47
    ATTN: Technical Information

Sandia Laboratories
    ATTN: G. Yonas
    ATTN: Orgn. 3141

DEPARTMENT OF DEFENSE CONTRACTORS

Avco Research and Systems Group
    ATTN: Library, A830

BDM Corporation
    ATTN: Corporate Library

Boeing Company
        ATTN: Aerospace Library

Dikewood Industries, Inc.
        ATTN: L. Davis

EG&G Washington Analytical Services Center, Inc.
        ATTN: Library

Ford Aerospace and Communications Corp.
        ATTN: Tech. Info. Services

General Electric Company
Space Division
        ATTN: J. Peden

General Electric Company-TEMPO
Center for Advanced Studies
        ATTN: DASIAC

Institute for Defense Analyses
        ATTN: Classified Library

IRT Corporation
        ATTN: R. Mertz

JAYCOR
        ATTN: E. Wenaas

JAYCOR
        ATTN: R. Sullivan

Kaman Sciences Corporation
        ATTN: W. Ware
        ATTN: A. Bridges
        ATTN: J. Hoffman
        ATTN: D. Bryce

Lockheed Missiles and Space Co., Inc.
        ATTN: S. Taimuty

Lockheed Missiles and Space Co., Inc.
        ATTN: L. Chase

Maxwell Labs., Inc.
        ATTN: A. Miller
        ATTN: P. Korn
        ATTN: A. Kolb

McDonnell Douglas Corporation
        ATTN: S. Schneider

Mission Research Corporation
        ATTN: W. Hart
        ATTN: C. Longmire

Mission Research Corporation-San Diego
        ATTN: V. Van Lint

Northrop Corporation
Northrop Research & Technology Center
        ATTN: Library

Northrop Corporation
Electronic Division
        ATTN: V. Demartino

Physics International Company
        ATTN: C. Stallings
        ATTN: S. Putnam
        ATTN: I. Smith
        ATTN: B. Bernstein
        ATTN: P. Spence
        ATTN: D. Dakin

R & D Associates
        ATTN: L. Schlessinger
        ATTN: W. Graham, Jr.
        ATTN: C. MacDonald
        ATTN: C. Fisher

Science Applications, Inc.
        ATTN: J. Beyster

Spire Corporation
        ATTN: R. Little

SRI International
        ATTN: S. Dairiki

Systems, Science and Software, Inc.
        ATTN: A. Wilson

Texas Tech. University
        ATTN: T. Simpson

TRW Defense & Space Sys. Group
        ATTN: Technical Information Center

Vought Corporation
Michigan Division
        ATTN: Tech. Information Center